8 Evolution of Solar and Intermediate-Mass Stars

Falk Herwig
Department of Physics and Astronomy, University of Victoria, Victoria, BC, Canada

Abstract: A brief discussion of the physics and numerical techniques for stellar evolution of solar and intermediate-mass stars is followed by a detailed description of the evolution of a $3\,M_\odot$ star from the main sequence through the red giant branch, He-core burning, and on to the thermal-pulse AGB evolution. He-shell flashes and the associated mixing as well as the nucleosynthesis are discussed, including the *s* process. Post-AGB evolution including post-AGB He-shell flashes are presented. Variations of the evolution as a function of mass, the initial–final mass relation, and lifetimes are summarized. Peculiarities of intermediate-mass AGB stars, hot-bottom burning, the super-AGB stars, as well as low-mass stellar evolution through the He-core flash are described in detail. The evolution of low- and intermediate-mass stars is presented. The final chapter covers some aspects of the dynamical star that are not well described in the spherically symmetric framework of stellar evolution.

1   Introduction

There are different ways in which stellar evolution can be grouped as a function of initial mass. The most obvious distinction is in terms of the final outcome. At solar metallicity stars more massive than ~$9\,M_\odot$ will eventually explode as a core-collapse supernova, while stars with initially smaller mass will end their lives as white dwarfs. At the low-mass end, stars only a little less massive than the sun will have lifetimes exceeding the age of the universe. For example, a star with initially $0.8\,M_\odot$ and a metal content of $Z = 0.01$ would ignite He only after ~2.2×10^{10} yr. While the detailed main-sequence evolution of such stars is important, for example, for the determination of ages in globular clusters, such low-mass stars would not yet have evolved through advanced stages and eventually into white dwarfs. However, especially these advanced stages, including the evolution following He-core burning, on the asymptotic giant branch (AGB) and through the He-shell flashes (or thermal pulses, to be used synonymously), are responsible for an important aspect of stellar evolution: the formation of the elements through nucleosynthesis.

The solar and intermediate-mass stars can therefore be defined as those which end their lives as white dwarfs. When studying the evolution of stars in this mass range, there may be different aspects to be interested in, which may be related to specific ways in which stars can be investigated through observations. For example, stars as members of populations and their appearance in the Hertzsprung–Russell diagram (HRD) or color-magnitude diagram are investigated through photometry or spectrophotometry. Such a diagram is shown in ❯ *Fig. 8-1* for a set of solar and intermediate-mass stars, and the features of these evolutionary tracks will be discussed in detail in this chapter. This area has now expanded into using abundance tracers to characterize stellar populations (e.g., Venn et al. 2004, for the case of dwarf spheriodal galaxies), aided enormously through the now common place use of multi-object, fiber optics spectroscopy. Another important avenue to investigate the physics and evolution of stars is asteroseismology, and new space missions, like NASA's Kepler mission, or previously the Canadian MOST satellite, provide data of unprecedented quality that allow probing directly the otherwise inaccessible mechanical properties of stellar interiors. A case of particular importance is of course the sun, which is very well studied through helioseismology.

Finally, stars reveal their internal workings through the surface abundances of elements, and in some cases isotopes, that can be measured spectroscopically. While stars, at least in the solar neighborhood, have formed out of material that is very similar in its composition compared to
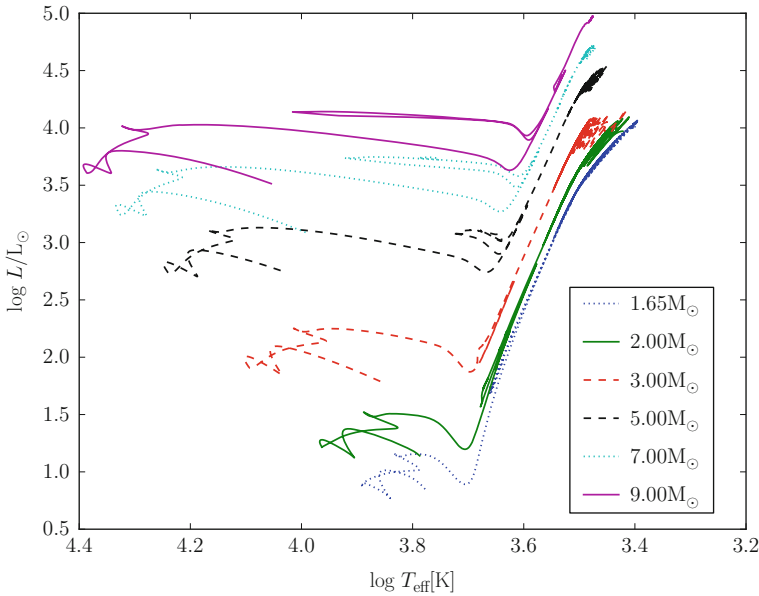
◼ Fig. 8-1

Hertzsprung–Russell diagram (HRD) for a range of masses metallicity Z = 0.02. Most of the pre-main sequence has been omitted for clarity. One-dimensional models during the very advanced thermal-pulse AGB phase show erratic behavior of the surface parameters due to pulsations that is not shown here for clarity; see text for discussion

the solar abundance distribution, many stars are known with very nonsolar abundance patterns. In most cases, these nonsolar abundance patterns are the result of internal nucleosynthesis processes in the deep stellar interior in combination with mixing processes that bring the nuclear burning products to the stellar surface. In some cases, observed abundance patterns are due to external contamination in a binary star system.

Binary stellar evolution cannot only lead to such a chemical pollution of a companion, but many binary stars will interact at some point in their lives. The evolution of such interacting binaries, for example, through a common envelope evolution (e.g., Ricker and Taam 2008; Passy et al. 2012) will lead to the formation of several types of very important systems, often involving at least one compact member. For example, the progenitor evolution of the important class of thermonuclear supernova (SN Type Ia) involves at least one binary interaction of this type. The impact of binarity on stellar evolution is treated elsewhere in ❯ Chap. 13.

The different ways of investigating stars through observations are complemented by theoretical investigation of stellar physics. The combination of theories and models of the many microscopic and macroscopic processes, that affect the evolution of stars, into computer simulations leads to quantitative models of stellar evolution. These are, under certain simplifying assumptions, as, for example, the assumption of spherical symmetry, able to quantitatively follow the global evolution of stars from their birth on the pre-main sequence through a series of nuclear burning stages and thermal transition phases all the way to their final white dwarf star destination.

These stellar evolution models are continuously improved, then confronted with observational properties of stars described above, and then again improved. This process, while easy to spell out in principle, is not always straight forward nor immediately successful. For example, helioseismology shows that the radiative, that is, non-convective interior of the sun rotates as a solid body, while the outer convectively unstable layers rotate differentially (Thompson et al. 2003). This is at odds with some models of the effect that rotation has in stellar evolution simulations, which assume rather effective transport of angular momentum in convection zones, enforcing near-solid body rotation there, while allowing for differential rotation in the inner layers of the sun that are not mixed through convection.

While the different observational approaches to investigate the evolution and nucleosynthesis in stars are mostly covered in other chapters of this book, this chapter describes the evolution and nucleosynthesis of solar and intermediate-mass stars as it presents itself according to the state of the art of global simulations of stars through computer simulations, that is, through stellar evolution computations. With all its limitations in mind (see previous paragraph for an example), a very detailed and in many ways probably realistic picture of the overall evolution, nucleosynthesis processes and yields, and final outcomes has emerged. And as the various aspects of this picture of stellar evolution will be presented, the many unsolved and open questions will be pointed out as well.

This chapter is organized as follows. In ❯ Sect. 2, the physics and to a limited extend the computational ingredients needed to construct realistic models of stars and their evolution, including the nuclear physics for the energy production and synthesis of the elements, are reviewed. Then, the evolution of a $3\,M_\odot$ star will be described from the main sequence all the way to the post-AGB phase (❯ Sect. 3). In ❯ Sect. 4, differences in the evolution of lower and higher mass stars are presented. The final section covers briefly evolution effects due to rotation and dynamical interactions between nuclear energy release and convective mixing, that is not well described within the usual one-dimensional stellar evolution framework assuming strict spherical symmetry (❯ Sect. 5).

2   The Physics for Stellar Evolution

The basic ingredients for stellar evolution models are known for many decades now, and the material is covered in great detail in textbooks, such as Cox and Giuli (1968), Kippenhahn and Weigert (1990), and Hansen et al. (2004), while Clayton (1968), Rolfs and Rodney (1988), and Iliadis (2007) are geared more toward nucleosynthesis and nuclear astrophysics. Habing and Olofsson (2004) deal specifically with all aspects of AGB stars.

Stellar evolution codes have been constructed since the first computers became powerful enough in the 1960s (e.g., Henyey et al. 1964; Hofmeister et al. 1964). Over time, many groups have built sophisticated simulation codes, including more detailed and realistic physics data and models and advancing the simulation capabilities to address stellar evolution in the most extreme conditions. A recent and comprehensive description of a modern multipurpose stellar evolution code was given by Paxton et al. (2011) for the MESA code, which can be downloaded – together with detailed instructions and examples – at http://mesa.sourceforge.net. That paper gives a complete technical account of the input physics and numerical techniques used in stellar evolution simulations today. However, the state of the MESA code described there did not include many of its more advanced capabilities yet, as, for example, modules that attempt to

account for the effect of rotation and magnetic fields. These aspects of stellar physics have been reviewed recently by Maeder and Meynet (2012) and will not be covered much in this chapter. With so many excellent resources available, this section will only attempt to provide a basic review of the most important concepts.

The conservation laws of mass, momentum, and energy can be written down in the following way (e.g., Clarke and Carswell 2003):

$$\frac{\partial \rho}{\partial t} + \nabla \cdot (\rho \mathbf{u}) = 0 \tag{8.1}$$

$$\rho \frac{\partial \mathbf{u}}{\partial t} + \rho(\mathbf{u} \cdot \nabla)\mathbf{u} = -\nabla p + \rho \mathbf{g}$$

$$\frac{\partial E}{\partial t} + \nabla \cdot \left[(E + p)\mathbf{u}\right] = \rho \dot{Q} + \rho \frac{\partial \Psi}{\partial t}$$

where $\mathbf{u}$ is the velocity, ρ the density, p the pressure, and the gravitational acceleration $\mathbf{g}$ is given by the gravitational potential Ψ ($\mathbf{g} = -\nabla\Psi$). The total energy per unit volume is $E = \rho\left(\frac{1}{2}u^2 + \Psi + \epsilon\right)$ and consists of the kinetic, potential, and internal energy. In each case, the left side of the equations represent the time variation of a quantity and the spatial transfer, while the right side contains sources and sinks. For the momentum, equation sources are the gravitational acceleration and the pressure force, for example, of the ideal gas. In the energy, equation Q represents all sources (e.g., from nuclear reactions) or sinks (e.g., from neutrino losses).

Solving this set of conservation laws numerically with high enough spatial and time resolution, and complemented with appropriate microphysics, allows in principle to simulate all possible behaviors of stars, except the effects of magnetic fields. However, in practice, this is not possible just like that. The reason is the vastly different time scales (as well as spatial scales) that interact in stars. These are the nuclear time scale, the thermal time scale, and the dynamical time scale, and although these are very basic concepts, they are so important that it is justified to briefly review them.

The dynamical time scale indicates how fast pressure fluctuations propagate and can be approximated by $t_{\mathrm{dyn}} \sim 1/\sqrt{G\bar{\rho}}$, where G is the gravitational constant and $\bar{\rho}$ is the average density of the star or region under consideration. For the sun, $t_{\mathrm{dyn}} \sim 1\mathrm{h}$. Another way to think of the dynamical time scale is to consider a star that suddenly looses its pressure support from the equation of state, like in a core-collapse supernova. The star will respond by collapsing on the dynamical time scale. Sound waves propagate through the star on the dynamical time scale. Other processes that would be considered dynamical, as, for example, the advection flows in convectively unstable parts of the star, are not proceeding on this dynamic time scale, but, in this example, on the convective turnover time scale. The thermal time scale is broadly speaking the time on which differences in internal energy or temperature equilibrate, and it is given by $t_{\mathrm{therm}} \sim \epsilon/L$, where ϵ is again the internal energy of a region of interest and L is the associated luminosity. The thermal time scale of the initial cooling of a pre-main-sequence star to the zero-age main sequence, when H-burning first starts, is called the Kelvin–Helmholtz time scale, and it is for the sun 1.5×10^6 yr. Finally, the fraction of nuclear fuel (e.g., H in the core of main-sequence stars) that provides energy ϵ_{nuc} to the star to temporarily halt further gravitational contraction will be depleted on the nuclear time scale $t_{\mathrm{nuc}} = \epsilon_{\mathrm{nuc}}/L$, which is of the order to 10^{10} yr for the sun. This global nuclear time scale determines the long-term evolution of stars in thermal and hydrostatic equilibrium. It needs to be distinguished from a nuclear reaction time scale of a particular reaction that may be compared with dynamical processes like convection.

The evolution time scale of solar and intermediate-mass stars is either the thermal or the nuclear time scale, depending on their evolutionary stage.

The evolution of stars is a typical example of a multi-physics, multi-scale problem where the properties of different types of physics on vastly different scales interact in a nonlinear way. ❯ Equation 8.1 allows for any pressure fluctuations, that is, sound waves, to propagate through the star. In particular, in the stellar interior, the sound speed ($v_s \sim \sqrt{P/\rho}$ for an ideal gas) is very high, and the Courant–Friedrich–Levy condition imposes in that case very short time steps (of the order $\Delta t = \Delta x / v_s$, where Δx is the chosen spatial grid size). In convective He-shell flashes, to be discussed in detail in ❯ Sect. 3.2, for example, the sound speed is ~1,000 km/s, and in present-day simulations that solve (❯ 8.1), explicitly this implies $\Delta t \sim 0.01$ s. However, the convective turnover time scale is of the order 1,000s while the evolutionary time (in this case, the thermal time scale) is ~100 yr. Similar arguments can be made for all other phases of stellar evolution, and also, the fact that some effort is going into implicit solution schemes does not alter the conclusion that it is not possible, and will not be possible in the foreseeable future, to simulate the entire evolution of stars by solving (❯ 8.1). This seems to be almost a trivial statement. However, it is important to keep in mind that the picture of the evolution of stars and their nucleosynthesis, that will be presented in subsequent sections, is based on simplifications of (❯ 8.1) and that there are a number of unresolved properties of stars that these simplified equations cannot accurately describe. Among these unresolved properties are many mixing processes, and these in turn are often essential for the quantitatively reliable description of nuclear production in stars.

In order to solve the conservation laws over the long thermal and nuclear time scales, (❯ 8.1) is solved implicitly assuming spherical symmetry and, in the Lagrangian coordinate m, the enclosed mass. The stellar evolution equations are therefore (e.g., Kippenhahn and Weigert 1990):

$$\frac{\partial r}{\partial m} = \frac{1}{4\pi r^2 \rho} \tag{8.2}$$

$$\frac{\partial P}{\partial m} = -\frac{Gm}{4\pi r^4} - \frac{1}{4\pi r^2 \rho}\frac{\partial^2 r}{\partial t}$$

$$\frac{\partial l}{\partial m} = \sum_i \epsilon_i$$

where r is the radius, l is the luminosity, and the ϵ_i stand for the various energy sources and sinks (see the chapter on stellar structure for more details). The implicit solution of these equations allows to advance an evolution sequence numerically with time steps of the order of a fraction of $\min(t_{\mathrm{nuc}}, t_{\mathrm{therm}})$. Often, the inertial term in the momentum equation is ignored since stars evolve in almost perfect hydrostatic equilibrium ($t_{\mathrm{dyn}} \ll \min(t_{\mathrm{nuc}}, t_{\mathrm{therm}})$). Indeed, whenever the inclusion of the inertial term is really necessary, the star is probably also violating the assumption of spherical symmetry. Most dynamic motions of fluid elements in stars are not spherically symmetric but turbulent. These issues will be discussed more in ❯ Sect. 5. Here, it is only important to fully appreciate that in real stars, there are relevant processes at work that are not described by (❯ 8.2).

In order to solve (❯ 8.2), the expression for the temperature gradient $\partial T/\partial m$ has to reflect the dominant mode of energy transport. In solar and intermediate-mass stars, three modes of energy transport are relevant. In convective layers, the temperature gradient is adiabatic, at least in the stellar interior. In the envelope where convection may be inefficient, or in convectively

stable layers, the temperature gradient is given by optically thick, gray radiation diffusion:

$$\frac{\partial T}{\partial m}\bigg|_{\text{rad}} = -\frac{3}{64\pi^2 \text{ac}} \frac{\kappa l}{r^4 T^3} \tag{8.3}$$

where κ is the Rosseland mean opacity or the electron conduction coefficient, a is the radiation-density constant, and c the speed of light. In the electron-degenerate cores (the white dwarfs to be) of solar and intermediate-mass stars in the advanced evolution stages, electron conduction dominates the energy transport.

The detailed microphysics entering modern stellar evolution calculations is described elsewhere. As an example, the options available in the MESA code are documented in Paxton et al. (2011). Radiative opacities depend on the assumed composition mix. Standard tables are available for solar or solar-scaled compositions. An important improvement was the introduction of tables with more general abundance mixes, in particular with enhanced C and O abundances (Iglesias and Rogers 1996). These allow a more realistic treatment of advanced stages of stellar evolution when the C and O abundance change due to nuclear burning and mixing processes. One of the results of the adoption of these more realistic opacity tables is the greater difficulty of computing advanced AGB models. The large opacity of C and O enriched AGB envelopes in high-mass loss phases at the tip of the AGB makes surface layers only weakly bound, and in this phase, the spherically symmetric simulation is at or past its application limit. Another import advancement has been the introduction of chemistry-dependent low-temperature molecular opacities (Marigo 2002; Cristallo et al. 2007; Weiss and Ferguson 2009; Marigo and Aringer 2009). In particular, when AGB stars become C-rich, the added sources of molecular opacity in this chemistry regime make the stars ~200–300 K cooler and probably boost mass loss through enhanced dust formation (❷ Sect. 3.2).

The equation of state of solar and intermediate-mass stars is dominated by either the ideal gas equation of state (including partial ionization where applicable) and the pressure from the degenerate electron gas in the cores in advanced evolution stages (❷ *Figs. 8-3* and ❷ *8-6*). Modern EOS routines combine tabulated data from different specialized sources that take nonideal effects appropriately into account (e.g., Paxton et al. 2011, for references).

The terms ϵ_i in (❷ 8.2) contain neutrino losses, for example, through plasmon decay and bremsstrahlung, that are important in the high-density environments of the degenerate cores in the advanced evolution stages of solar and intermediate-mass stars. In addition to this energy sink, the energy generation ϵ_{nuc} from nuclear reactions needs to be taken into account, and these are simultaneously responsible for composition changes:

$$\frac{d\mathbf{X}_j}{dt}\bigg|_{\text{burn}} = \hat{F}_j \cdot \mathbf{X}_j \tag{8.4}$$

where $\mathbf{X}_j$ is a vector containing the mass fractions of all species in zone j and the operator $\hat{F}_j$ represents all reactions through which these species can interact. Instead of in terms of mass fraction X, the network equations are rather written in terms of the number density N_m of species m by collecting all production and destruction terms of reactions of the type $k + l \rightarrow m + n$:

$$\frac{dN_m}{dt} = N_k N_l < \sigma v >_{kl,m} - N_m N_n < \sigma v >_{mn,o} + \ldots + N_i \lambda_{i,m} - N_j \lambda_{m,j} \tag{8.5}$$

where $<\sigma v>$ is the product of the cross section and the relative velocity in the center-of-mass system averaged over the appropriate distribution function and λ is the rate for β decays. Reaction rates can be obtained, for example, from (Angulo et al. 1999, http://pntpm.ulb.ac.be/Nacre/nacre_d.htm). The number density is expressed in terms of a number fraction or mole fraction $Y = X/A$, with A the atomic mass number, by $N = Y\rho N_A$ where $N_A = 1/M_u$ is the Avogadro number and M_u is the atomic mass number. For each reaction, an amount of energy Q is released, which is partly in the form of neutrinos and therefore lost. The energy released from ΔN reactions is therefore $\epsilon_{nuc} = \Delta NQ = \Delta Y\rho N_A Q$.

Typically, in a stellar evolution simulation, only a comparatively small network needs to be considered. It only needs to be large enough to take into account the reactions that are important for the energy generation. For stars that end their lives as CO-white dwarfs, this can be accomplished with approximately 15 species. A post-processing simulations can then take care of the many trace elements that are produced in stars but do not feed back into the thermal evolution, such as the *s*-process elements (❯ Sect. 3.2).

In addition to nuclear reactions, abundance changes are due to mixing processes, which are often taken into account in a time-dependent manner through a diffusion equation in the Lagrangian coordinates:

$$\left.\frac{dX_i}{dt}\right|_{mix} = \frac{\partial}{\partial m}\left[\left(4\pi r^2 \rho\right)^2 D(m)\frac{dX_i}{dm}\right] \tag{8.6}$$

where X_i is the radially dependent mass fraction of species i and D is a radially varying diffusion coefficient that reflects the different types of mixing in stars that the calculations take into account. The use of the diffusion equation is just a numerically convenient mathematical tool, whereas the processes treated in this way often have nothing to do with diffusion. Most mixing in stars is a result of convection, which is not a diffusion but an advection process. However, in practice, the mixing efficiency inside the convection zone is so high that one can even assume instantaneous mixing and the details of the mixing algorithm do not matter. But there are important exceptions, as, for example, when dealing with mixing due to rotation-induced instabilities (Maeder and Meynet 2012). It is also not clear if the partial mixing at convective boundaries is correctly described by a diffusion process. Finally, in situations where reactions are occurring fast compared to the convective turn-over and large-scale feedback of energy release from nuclear burning into the convective flow can be expected, the diffusion approximation is also probably not applicable (Herwig et al. (2011), see ❯ Sect. 5 for details).

Macroscopic processes that are responsible for mixing in single stars can be divided into two categories according to the time scale on which the driving mechanism operates. An efficient convection zone (e.g., in the deep stellar interior) has an adiabatic temperature stratification. Convection occurs in stars when energy transport through radiation alone is not efficient enough and the radiative temperature gradient (❯ 8.3) is larger than the adiabatic gradient. As can be seen from the nominator of (❯ 8.3), convective instability is triggered by a large luminosity, for example, from a burning shell in the interiors of stars during advanced phases of evolution, or because of large opacity, typically in the cool outer envelopes of stars, for example, during the red and asymptotic giant branch phase. Convective velocities are of the order of several km/s and lead to advective mixing that is fast compared to the evolutionary time scale of the star. Convection will also trigger mixing at or near convective boundaries, through overshooting, entrainment, or the excitation of internal waves in the stable layers neighboring the convection zones. These convection-induced mixing processes are already slower than

proper convective mixing. The three-dimensional and turbulent nature of convection can only be captured eventually by highly resolved numerical solutions of (❷ 8.1), while stellar evolution (❷ 8.2) needs to be supplemented with an approximate model of convection that is based on the available radially and temporal averaged, local values for the state variables. The simplistic model that is still used most often is the mixing-length theory (Böhm-Vitense 1958), and it has been pointed out that "one does not therefore expect quantitative results derived on the basis of this theory to have high accuracy or reliability" (Cox and Giuli 1968). Work to improve this situation is much needed and underway (e.g., Xiong et al. 1997; Canuto et al. 1996; Arnett et al. 2010) and supplemented by increasingly more realistic 3D simulations of convection (e.g., Porter and Woodward 2000; Browning et al. 2004; Freytag and Höfner 2008; Brun and Palacios 2009).

Even slower than that are mixing processes related to both thermal and abundance diffusivity or secular processes. These include thermohaline mixing and semi-convection where in the first case a thermally stable stratification is becoming unstable due to a destabilizing gradient of the mean molecular weight, or the other way around in the latter case. Despite renewed research effort (e.g., Charbonnel and Zahn 2007; Denissenkov 2010; Denissenkov and Merryfield 2011; Canuto 2011), these double-diffusive instabilities and the associated amount of mixing in stars are quantitatively not well understood, which represents another source of uncertainty in stellar evolution simulations. Rotation will induce mixing, for example, through meridional circulations or shear-driven flows (Endal and Sofia 1976; Pinsonneault 1997; Langer et al. 1999; Maeder and Meynet 2012). These slow mixing processes may be associated with velocities of the order of cm/s. Significant uncertainties exist in the quantitative treatment of mixing processes.

The physics ingredients of stellar evolution calculations briefly reviewed so far need to be complemented with a numerical solution scheme. Since the early days of stellar evolution, the solution scheme of choice has been a fully implicit Newton–Raphson scheme (Henyey et al. 1964), which is also adopted by the MESA code (Paxton et al. 2011). The three operators structure (❷ 8.2), mixing (❷ 8.6), and nuclear burn (❷ 8.4) may or may not be coupled in different combinations. Formally, the operators can be solved separately if the associated time scales are largely different. For solar and intermediate-mass stars, this is most of the times the case. Nevertheless, it is found that the fully coupled solution, that is adopted, for example, in the MESA code, seems to provide greater numerical efficiency and robustness. There are many additional numerical details, for example, concerning adaptive mesh refinement and boundary conditions that need to be addressed. At the end, a modern stellar evolution code can follow the entire evolution from the pre-main sequence to the white dwarf stars in a day or two on a present-day multi-core workstation. However, the difficulties of simulating the very advanced last thermal pulses on the AGB, as mentioned already above, remain (cf. ❷ Sect. 3.2).

3   The Evolution of a 3 M$_\odot$ Star

This section will describe the evolution of a 3 M$_\odot$ star according to the results of stellar evolution computations. This mass is representative of the lower-mass regime of CO-white dwarf progenitors which will experience the third dredge-up during the thermal-pulse AGB (❷ Sect. 3.2.1) and become C-rich and produce s-process elements. However, this mass avoids the complication of the He-core flash of lower initial mass, and it also avoids the effect of hot-bottom burning and C-ignition that is characteristic for more massive AGB stars. These additional evolutionary

options as a function of initial mass will be discussed in ❯ Sect. 4. Also, the evolution described in this section is for metallicity $Z = 0.02$, which is similar or maybe slightly higher compared to the sun's metallicity (Asplund et al. 2009). The evolution of stars with lower metal content has some peculiarities that will be presented in ❯ Sect. 5.

The evolution in the HRD is shown in ❯ Fig. 8-1. The 3 $M_\odot$ star evolves from the pre-main sequence toward the zero-age main sequence at $\log T_{\text{eff}} = 4.093$ and $\log L = 1.905$. Here it has its smallest radius and highest surface gravity, and the overall evolutionary trend for the star from hereon all the way to the tip of the AGB is to become cooler, more luminous, and, because $L = 4\pi R^2 \sigma T_{\text{eff}}^4$ (with σ the Stefan-Boltzmann constant), also larger, as is shown in ❯ Fig. 8-2.

Stellar evolution can be thought of as a continuous process of gravitationally induced collapse, temporarily halted by the ignition of and energy release from nuclear burning processes. The evolution of the central $\rho_c - T_c$ is shown in ❯ Fig. 8-3. In solar and intermediate-mass star evolution, advanced burning stages will be ignited off-center, due to the effect of neutrino cooling in the highest-density central locations. Nevertheless, the evolution of some key species involved in nuclear processes for energy generation in the center of the star is very instructive and demonstrates the temperature dependence of the different burning processes. Such a diagram is shown in ❯ Fig. 8-4 for the highest mass case discussed in this chapter, 9 $M_\odot$ (because only the highest mass eventually ignites C in the center). However, the ignition temperatures for the various nuclear burning processes are only weakly dependent on the density, and the corresponding 3 $M_\odot$ diagram would look similar.
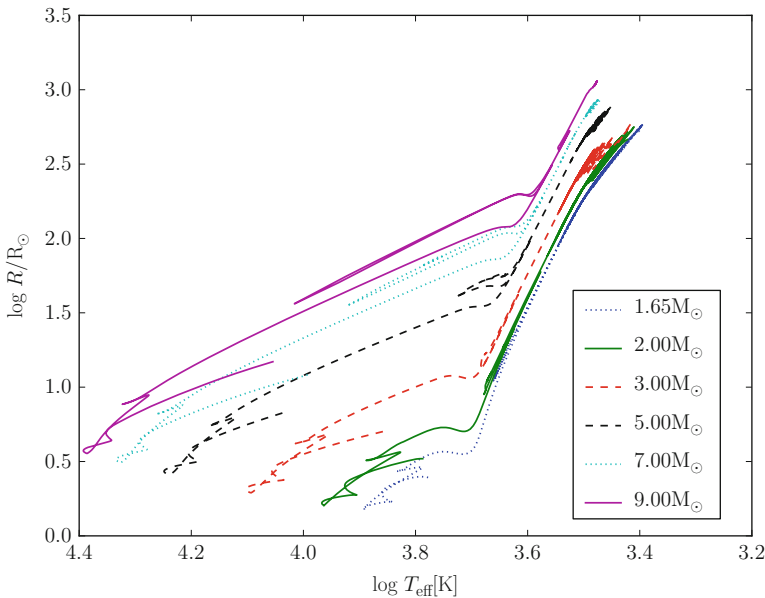
◾ **Fig. 8-2**

Same as ❯ *Fig. 8-1* but for the stellar radius. log T_{eff} – log R diagram for a range of masses with metallicity $Z = 0.02$
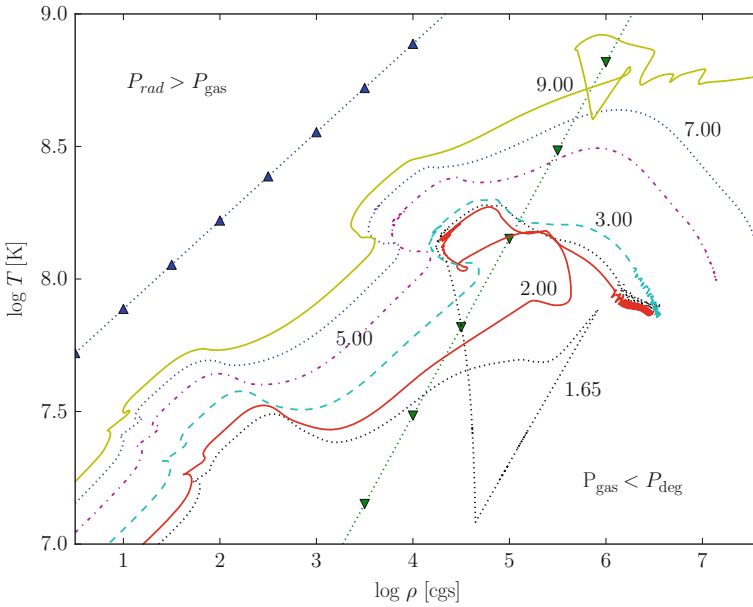
◨ Fig. 8-3

Evolution of the central density and temperature for the tracks shown in ❯ *Fig. 8-1*, plus a 7 and 9 M⊙ case. *Straight lines* with symbols divide areas dominated by radiation pressure, gas pressure, and the area dominated by the equation of state of degenerate electrons

Abundances profiles of for key species of the reaction network are given for representative evolution stages of the internal evolution in ❯ *Fig. 8-5* and are complemented by profiles in the $\rho_c - T_c$-diagram (❯ *Fig. 8-6*).

Furthermore, the so-called Kippenhahn diagram shows the time evolution of the mass coordinate of convection zones as well as in this case the mass coordinate of the H-free core and the He-free core (and for the highest mass cases also the ^{12}C-free core). All three mass coordinates are defined in this chapter as the smallest mass coordinate where the mass fraction of the respective species is $X < 10^{-4}$. These lines correspond either to the location of the nuclear burning shell or, in the case of a dredge-up process, to the location of the bottom of the convection zone that causes the dredge-up. A Kippenhahn diagram for the 3 M⊙ case is shown in ❯ *Fig. 8-7*.

3.1 Pre-main Sequence to the End of He-Core Burning

Stars form on the pre-main sequence in the cool and luminous part of the HRD. Because they are cool, the opacity is high and they are throughout convectively unstable. For that reason, they are well described by a polytrope with the index $n = 3/2$ of an adiabat. During this phase without significant nuclear energy sources, the star contracts on the short Kelvin–Helmholtz time scale (❯ Sect. 2). This short-lived convection therefore only shows up as a vertical line at $\log(t_{\text{final}} - t) = 8.68$ in ❯ *Fig. 8-7*.
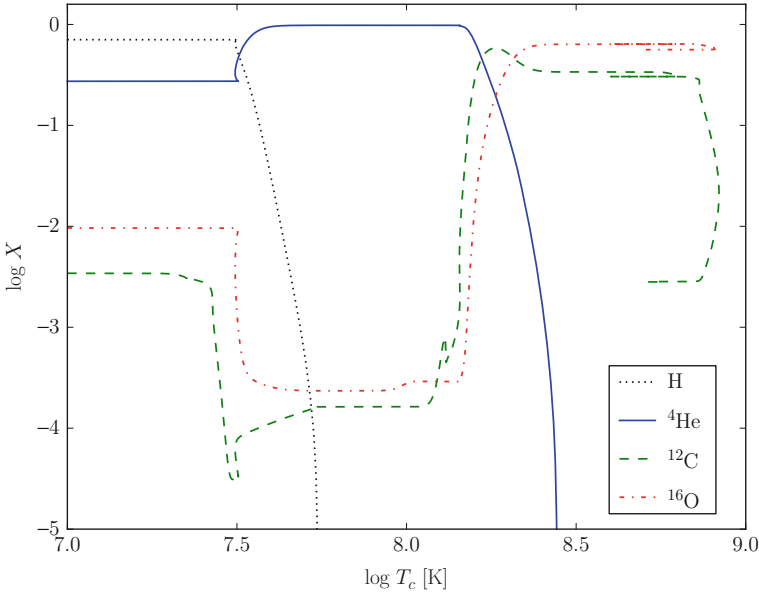
◼ Fig. 8-4

Evolution of the central mass fractions of key isotopes that trace the main nucleosynthesis processes, as a function of the central temperature for the $9\,M_\odot$, $Z = 0.02$ stellar evolution track. The major nuclear burning stages evident in the abundance variations cause prominent features in the $\rho_c - T_c$ diagram ◉ *Fig. 8-3*. This super-asymptotic giant branch star is right at the border to the massive star regime, and hence, C-ignition causes the ^{12}C abundance to decrease at the highest temperature (see ◉ Sect. 4)

◉ *Figure 8-4* shows that core H-burning takes place at $\log T = 7.5$ in the $9\,M_\odot$ stellar model. For the $3\,M_\odot$ star H burns already at $\log T = 7.4$ and $\log\rho = 1.6$. The ignition of H in the center causes a characteristic feature in the $\rho_c - T_c$-diagram (◉ *Fig. 8-3*). The central evolution toward higher ρ and T is halted during the major core burning phases. The $\rho_c - T_c$ profile (◉ *Fig. 8-6*) which also features markers for mass coordinates shows that the innermost $0.65\,M_\odot$ are relatively compact and have only small dynamic range in density and temperature.

In these higher-mass stars, H-burning proceeds via the CNO cycle that depends on the availability of C, N, and O isotopes as a catalyst. The basic cycle involves p-captures on ^{12}C, ^{13}C, ^{14}N, and the ^{15}N$(p,\alpha)^{12}$C reaction that closes the cycle. The relative abundances of the CNO isotopes are reshuffled during CNO cycling so that ^{14}N, which has the largest Coulomb barrier and therefore the smallest p-capture cross section, has the highest abundance in CNO-cycle H-burning ashes (Arnould et al. 1999). This can be seen on the left of the top panel in ◉ *Fig. 8-5* that shows the central region of the $3\,M_\odot$ during the main sequence. The initial (solar-scaled) abundance distribution can be seen on the right side of that panel, which shows the unprocessed and at this point also still unmixed surface composition. There, ^{16}O dominates the CNO isotopes. The workings of the CNO cycle can also be seen in ◉ *Fig. 8-13*, which shows a H-burning situation in a later phase of the evolution. However, the CNO cycle is the same, and the profiles show the signatures of the various reactions, being activated from lower to
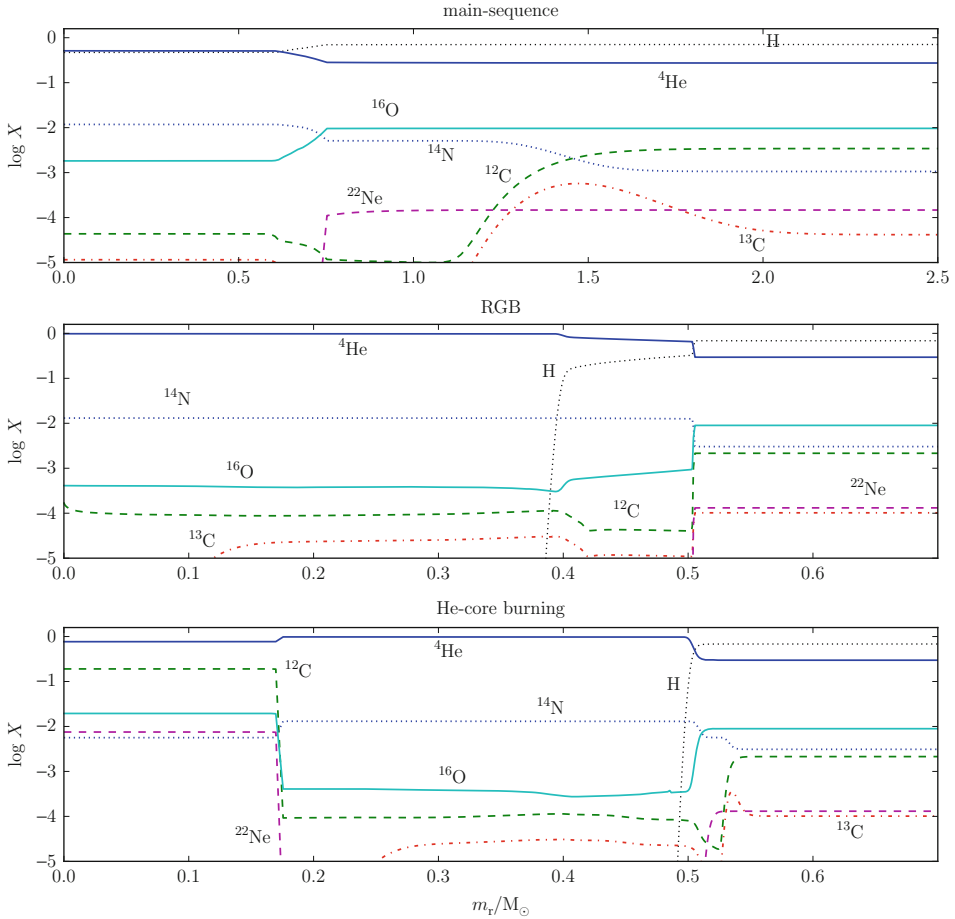
◼ Fig. 8-5
Abundance profiles for the same evolutionary stages as shown in ❯ *Fig. 8-6* (except the AGB profiles, which will be described in detail later, e.g., ❯ *Fig. 8-14*). The evolutionary stages shown at times log $t_{final} - t$ = 8.45, 8.04, 7.91 (*top* to *bottom*) on the scale used in ❯ *Fig. 8-7*

higher temperatures from the right (outer layers) to the left (layers further inward). The effect of H-burning via the CNO cycle is to turn most ^{16}O and ^{12}C into ^{14}N. This will be important, as shown in later sections, for the *s* process.

Nuclear reaction rates have a high temperature dependence, which means that nuclear burning is confined only to the most central region where the temperature peaks. Despite that, the abundance profiles are flat in the central region of the main-sequence star (top panel in ❯ *Fig. 8-5*), because that core region is convectively unstable and therefore well mixed. As shown in the Kippenhahn diagram (❯ *Fig. 8-7*, log($t_{final} - t$) = 8.68–8.07), the convection zone is decreasing in mass extent. This explains the shallow slope of the abundance profile of species like H, He, and ^{16}O (❯ *Fig. 8-5*) between m_r = 0.61 and 0.75 M$_\odot$. The slope is preserving the central abundances as a function of time according to the decreasing convective core.

While nuclear energy generation during the main sequence is restricted to the central region, more nucleosynthesis with consequences that are eventually observable is taking place in layers further out in the star. These layers are convectively stable (radiative), and in the stellar evolution models no mixing takes place. Therefore, even slow, nonequilibrium nucleosynthesis can build up abundance features. In particular, around $m_r \sim 1.5\,M_\odot$, a layer with enhanced ^{13}C results from the activation of the first reactions in the CN cycle: ^{12}C$(p,\gamma)^{13}$N$(^+\beta)^{13}$C$(p,\gamma)^{14}$N. During the subsequent red giant branch (RGB) or first giant branch phase, when a deep convective envelope emerges, this ^{13}C-bump will be mixed throughout the envelope (middle panel, ❷ *Fig. 8-5*) and to the surface where it leads to an observed decrease of the ^{12}C/^{13}C abundance. This first convective mixing of nuclear processed material to the surface due to a deepening envelope convection zone is called the first dredge-up. The second (❷ *Figs. 8-23* and ❷ *8-24*) and third (❷ *Figs. 8-9* and ❷ *8-10*) dredge-up are encountered after the end of He-core burning and after the end of He-shell flashes, respectively.

When H in the center is exhausted, the main-sequence phase ends, which in the HRD is the case at $\log T_{\text{eff}} = 3.956$ and $\log L = 2.142$. A characteristic switchback feature marks the terminal age main sequence and the transition from core H-burning to H-shell burning. The location of the H-shell is now tracked by the line for the H-free core in the Kippenhahn diagram (❷ *Fig. 8-7*). The core, not supported anymore by nuclear burning, contracts; H-burning starts in the shell, and the outer layers expand. The model star evolves at almost constant luminosity from the tip of the main sequence to the bottom of the RGB at $\log T_{\text{eff}} = 3.698$ (adopted here to be at the local minimum of L at $\log L = 1.177$), and this readjustment on the thermal time scale lasts 3.684×10^6 yr. At this stage, the H-burning shell is located at $m_r = 0.305\,M_\odot$. Because of the decreasing temperature in the envelope, the opacity increases and the outer layers become unstable against convection (❷ 8.3). At the bottom of the RGB, the bottom of the convective envelope has reached $m_r = 2.617\,M_\odot$ (❷ *Fig. 8-7*, at $\log(t_{\text{final}} - t) \sim 8.049$).

The star now evolves on the RGB, with an inert He core, a H-burning shell, and further out a large convective envelope. The structure has dramatically changed compared to the main-sequence configuration, as can be seen by comparing the $\rho_c - T_c$ profiles (❷ *Fig. 8-6*). The dynamic range between the three marked mass coordinates has significantly increased. The profiles shown in ❷ *Figs. 8-5* and ❷ *8-6* are taken when the stellar evolution track has almost reached $\log L = 2.602$ which is very close to the tip of the RGB at $\log L = 2.666$ for the $3\,M_\odot$ track. He-core burning is about to start, and in fact, a tiny uptick of the ^{12}C abundance can already be noticed in the center (middle panel, ❷ *Fig. 8-5*). ^{13}C is already gone because of the ^{13}C$(\alpha,n)^{16}$O reaction.

While the $0.35\,M_\odot$ mark is in the He core just below the H-burning shell at $0.393\,M_\odot$, the $0.5\,M_\odot$ mark is located just below the bottom of the convective envelope, while the $0.65\,M_\odot$ mark is well inside the convective envelope. The location of these markers on the $\rho_c - T_c$ profiles demonstrates the large density and temperature contrast between the core and the envelope in giant stars. This contrast is even more extreme in the AGB stars.

The H-burning shell is relatively shallow, compared to lower-mass RGB stars, with a gently sloping H-profile between the H-burning shell and the bottom of the convective envelope. The latter is characterized by steep abundance gradients and flat profiles above. In the layer beneath the convective envelope, ^{22}Ne is destroyed by H-burning via the Ne-Na cycle.

The evolution from the bottom to the tip of the RGB (i.e., from the minimum to the maximum in L) takes 7.99×10^7 yr. The RGB profile shown in ❷ *Figs. 8-5* and ❷ *8-6* is at 5.91×10^6 yr before the RGB tip, when the He core has reached a mass of $0.400\,M_\odot$ and He ignites in the core. In the $9\,M_\odot$ star, this happens at $\log T \sim 8.17$ (❷ *Fig. 8-4*) while in the $3\,M_\odot$ case, He-core burning starts at $\log T \sim 8.06$. The core becomes convectively unstable because of
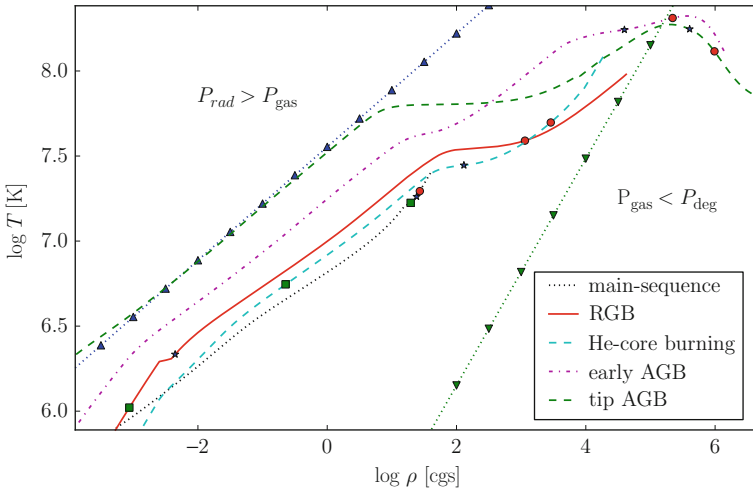
◩ Fig. 8-6
**Density-temperature profiles for the 3 M$_\odot$ stellar evolution track for the evolutionary stages shown
at times log t_{final} − t = 8.45, 8.04, 7.91, 6.23, and 3.38 (in the order in which the lines appear in the
legend) on the scale used in ❷ *Fig. 8-7*. The marks along each profile indicate the enclosed mass
0.35 (*red circle*), 0.5 (*blue star*), and 0.65 M$_\odot$ (*green square*). *Straight lines* with *triangle up* and *down*
marks divide areas dominated by radiation pressure, gas pressure, and the area dominated by the
equation of state of degenerate electrons**

the large energy generation from He burning. In the next 7.01×10^6 yr, the model star evolves to
below 100 L$_\odot$. This is a typical luminosity for the He-core burning phase which lasts 1.02×10^8 yr
and ends at $\log(t_{\text{final}} - t)6.967$ in ❷ *Fig. 8-7*.

The ignition of He produces again a characteristic feature in the $\rho_c - T_c$ evolution, similar
to when H ignited. Compared to the RGB, the density has decreased in the center, and the tem-
perature has increased. The star is again more in a dwarflike configuration with a much smaller
range in temperature and density from the center to the surface, compared to the giant con-
figuration. The Kippenhahn diagram shows that the convective envelope has receded and the
bottom of the convection zone reaches a maximum mass coordinate of 2.30 M$_\odot$. The abundance
profile (bottom panel, ❷ *Fig. 8-5*) shows how ^{12}C is forming from the triple-α reaction. Several
other He-burning reactions are now activated in the core, including ^{12}C$(\alpha, \gamma)^{16}$O as well as the
α-capture chain ^{14}N$(\alpha, \gamma)^{18}$F$(^+\beta)^{18}$O$(\alpha, \gamma)^{22}$Ne. In massive stars, this reaction chain trans-
forms ^{14}N from the CNO cycle into the neutron source ^{22}Ne $(^{22}$Ne$(\alpha, n)^{25}$Mg), and in
those stars, this ^{22}Ne plays an important role for the weak s process. However, in solar and
intermediate-mass stars, this core material will be eventually buried in the white dwarf. The
relevant nuclear production site for the s process is during the AGB stage.

During the He-core burning phase, H burning continues in the shell. The H-free core
reaches 0.57 M$_\odot$ at the end of He-core burning, and throughout this phase, the luminosity from
H burning exceeds the He-burning luminosity for this initial mass. Contrary to the core con-
vection zone during H-core burning, the convective core during He-core burning grows. In
this particular situation, the radiative and adiabatic gradients outside the proper core convec-
tion region have about the same value within a mass shell of mass ≤0.05 M$_\odot$ due to opposing
trends impacting the radiative gradient with an outward decreasing luminosity and increasing
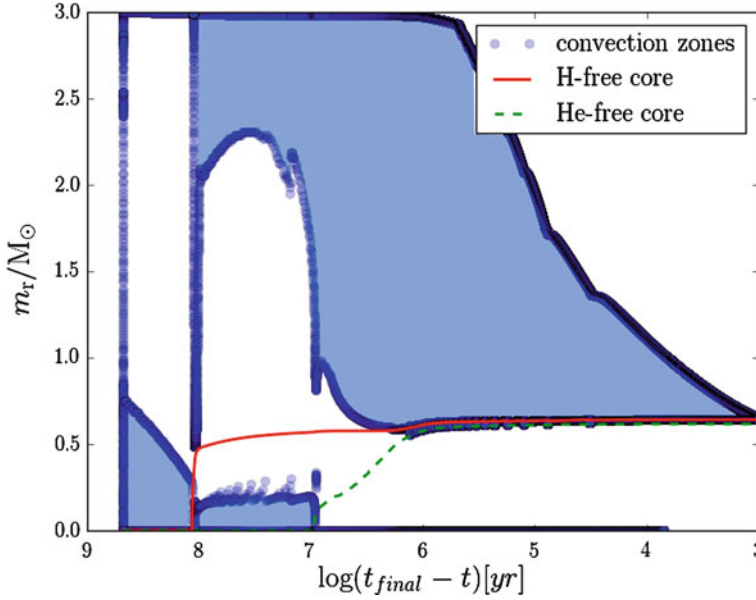
◼ Fig. 8-7
Kippenhahn diagram of M_{ZAMS} = 3 M$_\odot$ stellar evolution calculation with Z = 0.02 from the pre-main sequence to the end of the TP-AGB evolution when all envelope mass is lost. The position of convection zones and the mass coordinate below which the star is H- and He-free is shown as a function of reverse logarithmic time. In this way, the abscissa represents the logarithm of the time left until the end of the AGB evolution, which is reached when almost all the envelope mass is lost and the star will leave the giant branch and evolves into the central star of a planetary nebula (❯ Sect. 3.2)

opacity. This is a case where secular instabilities (in this case semi-convection) that were discussed in ❯ Sect. 2 play a role. This introduces an uncertainty for post-He-core burning core masses. When the He in the center is completely transformed into ^{12}C and ^{16}O, He-core burning is finished.

3.2   Asymptotic Giant Branch Evolution

The events after the end of He-core burning are very similar to those at the end of the main-sequence evolution. The core resumes contraction while He-burning now switches to a shell. As a response to the contracting core, the envelope expands again, and the envelope convection deepens again. This and the subsequent evolution along the early AGB up to the thermal pulses are shown in ❯ Fig. 8-8. In stars below $M_{ZAMS} \lesssim 3.5$ M$_\odot$, the bottom of the convective envelope will not penetrate into the H-free core (when this does happen, it is referred to as the second dredge-up, ❯ Figs. 8-23, and ❯ 8-24).

In the $\rho_c - T_c$ diagram, both the evolution of the central conditions (❯ Fig. 8-3) as well as the profile for the early AGB and even more so the tip AGB star (❯ Fig. 8-6) take a turn into
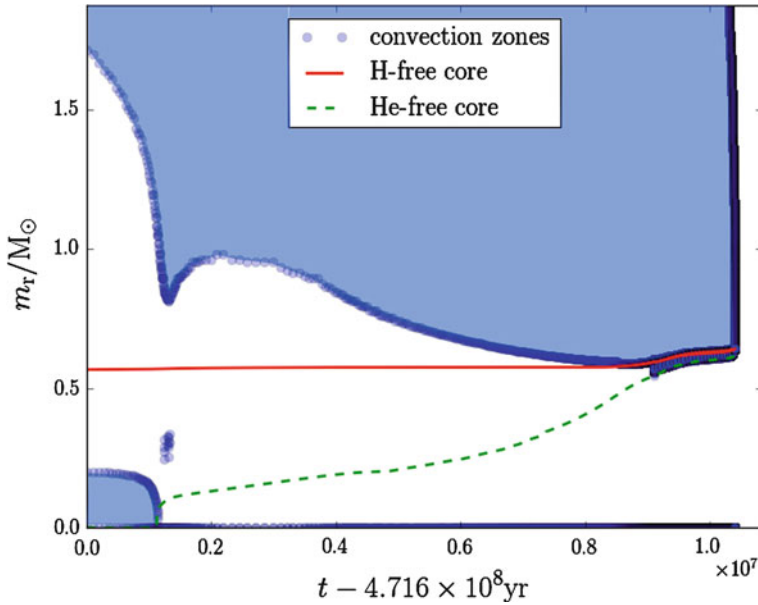
◼ Fig. 8-8
Kippenhahn diagram of M_{ZAMS} = 3 $M_\odot$ evolution from the end of core He burning through the early AGB to the end of the thermal-pulse AGB. The wiggles at the *bottom* of the convective envelope at ~0.6 $M_\odot$ on the *right* end of the diagram are the thermal pulses. On the time scale of this diagram, the envelope is lost through winds at an instant (cf. ❯ *Fig. 8-7*)

the regime dominated by the electron degenerate equation of state. The temperature decreases toward the center and in the center as function of time. Neutrino losses extract so much energy from the central region so that C burning, which would be the next nuclear burning process, cannot ignite. What will become eventually the white dwarf, an inert CO core supported through the pressure from degenerate electrons, starts to form after the end of He-core burning.

Contrary to the He-core burning phase, the He-burning luminosity from the He shell now by far exceeds the H-shell luminosity during the early AGB. In fact, the main thing that happens during this transition phase is the catching up (in mass coordinate) of the He-shell with the H-shell. Once the two shells are close to each other in mass, they start to interfere with each other, which leads to the He-shell flash or thermal-pulse phenomenon. As can be seen from the $\rho - T$ profiles (❯ *Fig. 8-6*), the model star has turned again into a giant configuration, and the envelope continues to expand as the core contracts. The phenomenon, that in stars with nuclear shells the envelope does the opposite of what the core does, is also known as the mirror principle (Kippenhahn and Weigert 1990). For the early AGB star, the 0.65 $M_\odot$ mass coordinate is already at such low density and temperature that it falls out of the range of the diagram. More quantitative details on the early AGB evolution can be found in Forestini and Charbonnel (1997).
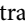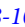
3.2.1 Thermal-Pulse AGB

Once the mass coordinate of the He-free core has approached the location of the H-free core to within ~0.04 $M_\odot$, the conditions for He-shell flashes are given. The He-burning shell is feeding on the ashes of the H-burning shell. For both to be burning stable in a steady-state manner, the He shell would have to process the same amount of mass that the H shell is producing as ashes. For this to happen, the conditions would have to be fine-tuned in an unlikely way, and stellar evolution simulations have not found any cases with simultaneously stable H and He burning.

He-Shell Instability
Instead, once the He shell has approached the H-burning shell in mass coordinate toward the end of the early AGB, H burning will take over the lead in energy production. The H-burning shell will support a lot of the pressure from the overlying envelope mass, and the temperature in the layer below does not allow full-blown He burning. He continues to be accreted from the H shell above and is accumulating. The region of the He shell is contracting and compressed due to the lack of energy production. The He shell is getting geometrically thinner, considering that the shell region is defined as the region between the absence of fuel at the bottom and the absence of high enough temperature at the top. Depending on the mass, this region will also become increasingly degenerate. In the 3 $M_\odot$ evolution track, the thin-shell instability will eventually trigger the He-shell flash. The basic idea is that with very little volume in the shell, at the onset of He-burning via the triple-α reaction with a very-high-temperature exponent, an increase of the energy generation cannot immediately lead to an expansion via PdV work. Locally and temporarily, the pressure is effectively decoupled from the temperature, which results in a thermonuclear runaway. A complete and more rigorous analysis taking also into the account the effect of degeneracy is given by Yoon et al. (2004).

The He-shell flash instability plays a central role in the final evolution of solar and intermediate-mass stars. They cause periodic convective mixing of the intershell, which is the region between the He and H shell. And they cause the third dredge-up mixing that brings the bottom of the convective envelope down into the intershell and, like the previous dredge-up episodes, mixes processed material from the intershell to the surface. The thermal pulses (the terms thermal pulse and He-shell flash are used synonymously) also trigger mixing episodes that are critical for the activation of the neutron source reactions $^{13}C(\alpha, n)^{16}O$ and $^{22}Ne(\alpha, n)^{25}Mg$. These processes will now be described in some detail, while an in-depth coverage of thermal-pulse AGB evolution has been given by Herwig (2005).

He-shell flashes are recurrent. ❯ *Figure 8-9* shows the complete series of flashes for the 3 $M_\odot$ evolution track, while ❯ *Fig. 8-10* provides details of the 12th thermal and the subsequent interpulse and 13th thermal pulse. The interpulse time, the time between thermal pulses, depends on the core mass (Forestini and Charbonnel 1997). For the advanced thermal pulses shown in ❯ *Fig. 8-10*, our simulation has an interpulse time of $t_{ip} \sim 6 \times 10^4$ yr. Models with higher core mass have shorter interpulse time.

Other global quantities of the AGB thermal-pulse evolution are also strongly correlated with the core mass, such as the luminosity (Paczyński 1970; Herwig et al. 1998; Marigo 2000) or the third dredge-up (Karakas et al. 2002). For example, Blöcker (1993, cited from Herwig et al. 1998) gives the following core-mass luminosity relationship:

$$L/L_\odot = 62,200(M_H/M_\odot - 0.487) . \tag{8.7}$$
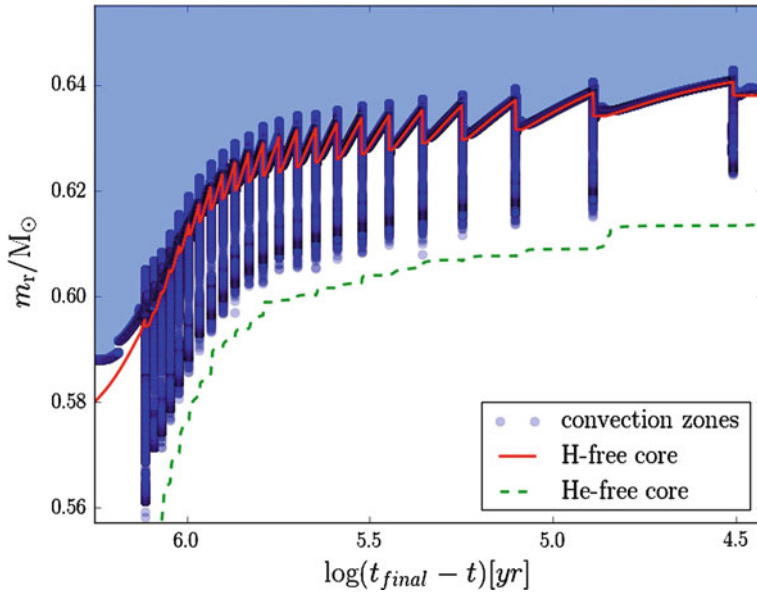
◨ Fig. 8-9
Zoom-in of Kippenhahn diagram ▶ *Fig. 8-7*, showing the sequence of thermal pulses. Sections where the mass coordinate of the H-free core increases correspond to H-shell burning phases, while a decrease of the H-free core indicates mixing of processed material from the intershell region (between the H- and He-free core) into the envelope via the third dredge-up
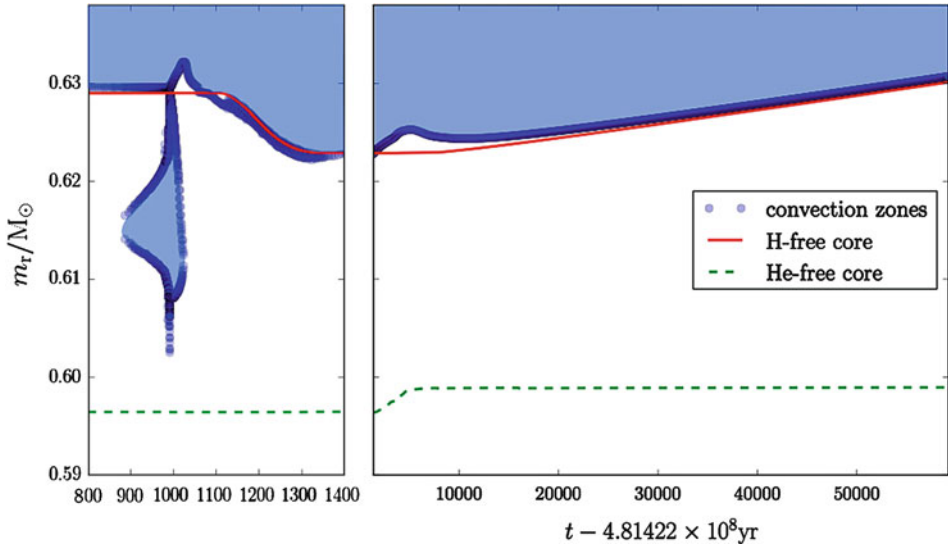
◨ Fig. 8-10
Kippenhahn diagram of the 12th thermal pulse (*left panel*) and the following interpulse phase (*right panel*). Note the different time scale for the two panels. The thermal pulses are very short compared to the interpulse phase

This so-called asymptotic behavior has motivated the construction of synthetic AGB models. These do not solve the full set of stellar evolution equations (❯ 8.2) but describe the properties of full stellar models through fitting formula of key quantities, such as the temperature in nuclear processing regions (e.g., Renzini and Voli 1981; Groenewegen and de Jong 1993; Marigo 2001).

Mass Loss

The total number of thermal pulses in an AGB sequence will be determined by the assumed mass loss. Mass loss will depend on the stellar mass, the temperature, the luminosity, the surface chemistry, and the envelope pulsations. It is the result of a complex interplay between mechanical driving of the circumstellar envelope through stellar pulsations, the formation of molecules and dust in the hydrodynamic environment of the stellar surface as well as the interaction of radiation with all involved constituents, and the transfer of moment between dust and gas (Willson 2000). Recent self-consistent modeling efforts are quite promising (e.g., Wachter et al. 2002; Mattsson et al. 2010). Observational determination of mass loss rates is indirect and therefore difficult (Jura and Kleinmann 1989, 1992; Groenewegen and de Jong 1998; van Loon et al. 1999; Olofsson et al. 2002). AGB stars will start the thermal-pulse phase with an O-rich surface composition (M star) left over from the initial composition. During the advanced thermal pulses, due to the dredge-up of primary C from the He-shell, lower mass AGB stars, like the $3\,M_\odot$ case, star will eventually become C-rich (see below and ❯ *Fig. 8-12*). The lower-mass M stars have to be distinguished from the much more luminous massive AGB stars that are O-rich because of hot-bottom burning (❯ Sect. 4). Larger and more homogeneous observational samples are now obtained, and the emerging picture (Olofsson 2003; van Loon 2005; De Beck et al. 2010), in very broad terms, is that the low-luminosity O-rich stars (and S stars which have a C/O ratio around unity) have mass loss rates in the range $-7.5 < \log \dot{M}/M_\odot \lesssim -6$, whereas the mass loss rate of C-stars are systematically higher, $-6.2 \lesssim \log \dot{M}/M_\odot \lesssim -4.8$. The massive O-rich AGB stars have on average even higher mass loss in the range $-5.5 \lesssim \log \dot{M}/M_\odot \lesssim -4.2$.

For the $3\,M_\odot$ stellar model, it is therefore expected that only a small fraction of the mass will be lost in the O-rich phase, while the C/O ratio gradually increases with each third dredge-up event (❯ *Fig. 8-12*) until the higher mass loss rate for C-rich stars kicks in. With an assumed average mass loss rate of $\log \dot{M}/M_\odot \sim -5.5$ out of the range for C-rich stars, the envelope mass of $M_{\text{env}} \sim 2.3\,M_\odot$ of the $M_{\text{ZAMS}} = 3\,M_\odot$ models star will be lost in $\sim 7 \times 10^5$ yr. With the interpulse time t_{ip} from ❯ *Fig. 8-10*, one can expect of the order of one dozen thermal pulses in the C-rich phase before all the envelope mass is lost, and the star will evolve off the AGB. In fact, the 12th thermal pulse shown in ❯ *Fig. 8-10* corresponds to the thermal pulse after which the envelope composition becomes C-rich, and therefore, a $3\,M_\odot$ star will have of the order 20–25 thermal pulses. The situation would be very similar for a $2\,M_\odot$ case.

Although observational and theoretical investigations of mass loss of AGB stars are making swift progress, the differences in adopted mass loss rates in stellar evolution simulations of different groups are still one of the major sources of uncertainty. Mass loss rate prescriptions used in stellar evolution simulations, if they are not entirely based on simulation based data, should take advantage of the well-established correlation of mass loss and pulsation period, as pointed out by Vassiliadis and Wood (1993). These authors, and approximately at the same time Blöcker (1995a), presented a large set of detailed AGB thermal-pulse stellar evolution calculations, followed all the way from the main sequence, through a large number of thermal pulses, and including mass loss. Such stellar evolution grid sets have been frequently updated now, with improved microphysics and more elaborate treatment of nucleosynthesis

(e.g., Forestini and Charbonnel 1997; Weiss and Ferguson 2009; Karakas 2010) and a lot of work that has specifically focused on lower metallicity, see ❯ Sect. 5.

In one of the previous paragraphs, the *primary* production of C was mentioned. In this context, a species is produced in a primary mode if it can be made only out of H and He (most of which in the solar abundance mix is still from the Big Bang) or, in other words, if the production does not directly depend on the presence of metals (anything not H or He) from a previous generation of stars. *s*-process elements depend on the presence of Fe from previous star generations as a seed and are therefore a secondary production, even if the neutron source may be primary (see below).
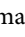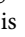
He-Shell Flash Mixing and Third Dredge-Up

He-shell flashes follow a sequence of events that is demonstrated in ❯ *Fig. 8-10* where the evolution of convection zones is shown, and ❯ *Fig. 8-11* shows the evolution of the H- and He-burning luminosity and the surface parameters. The He-shell flash starts during the preceding quiescent intershell phase when the stellar luminosity is almost entirely provided by the H shell. He is accreted onto the CO core, and eventually, the He-burning luminosity starts to increase. This leads via the instabilities described above into a thermonuclear runaway, and the He-burning luminosity rapidly increases to 10^7–10^8 $L_\odot$ (❯ *Fig. 8-11*). Due to this high local luminosity, the region just above the shell becomes convectively unstable (❯ 8.3). The mass extent of the He-shell flash convection zone grows both inward and outward until the entire intershell region is convectively unstable and therefore well mixed (left panel, ❯*Fig. 8-10*). Most of the energy will go into expansion work of the intershell layers and immediately above. The layer in which the H-shell is located will be lifted and cools, and the temperature decreases below the limit for H-burning. The H-burning luminosity drops to insignificant values (❯ *Fig. 8-11*). Not only the H-shell will extinguish as a result of the lifting and cooling of those outer layers but also the opacity will increase. Then, again, the radiative gradient will increase making the
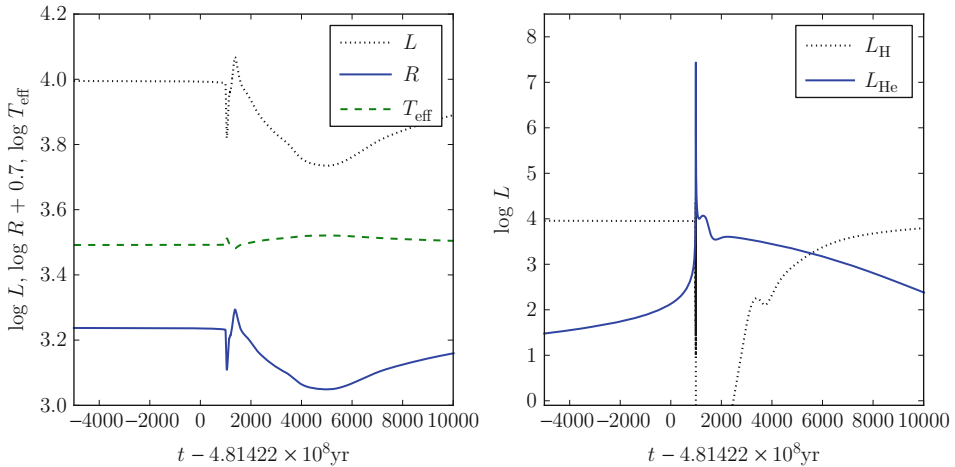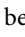

■ Fig. 8-11

Left panel: Surface parameters *R*, *L*, and T_{eff} before, during, and after the 12th He-shell flash of the 3 $M_\odot$, *Z* = 0.02 stellar model track; *right panel*: luminosities of H burning and He burning. The time axis is the same as in ❯*Fig. 8-10*

layer convectively unstable, and the mass coordinate of the bottom of the convective envelope will decrease (at ~−0.625 $M_\odot$ and time mark ~1,200 yr). This is the third dredge-up.

Both the formation and evolution of the He-shell flash convection and the dredge-up episode afterward proceed on the local thermal time scale of 150–200 yr, which will depend on the core mass. As seen from ❯ *Fig. 8-10*, the envelope convection overlaps in mass with the former location of the He-shell flash convection, between the largest extent of the top of the He-shell flash convection zone at 0.6288 $M_\odot$ (time marker 990 yr) and the deepest penetration of the bottom of the envelope convection zone at 0.6222 $M_\odot$ (time marker 1,300 yr). The mass difference $\Delta M = 6.6 \times 10^{-3}$ $M_\odot$ is the amount of processed material from the convectively mixed intershell that will be brought into the envelope. Therefore, a significant dilution factor of the order $\Delta M/M_{env}$ will have to be taken into account when deriving observable enhancement factors from admixture of enriched materials from the intershell due to the third dredge-up (for an example of such a mixing model, see Herwig et al. 2003). The effect of the third dredge-up can be seen in all of the Kippenhahn diagrams of this section, whenever the (red solid) line showing the location of the H-free core goes down. The sawtooth shape of that line in ❯ *Fig. 8-9* is therefore reflecting the growth of the H-free core due to H-shell burning during an interpulse phase, followed by a decrease of the H-free core during a third dredge-up event. The ratio of the amount of decrease (dredge-up mass) and increase (core growth mass) is called the dredge-up parameter λ. Whenever it is ~1, the core effectively does not grow anymore.

The third dredge-up will bring to the envelope all materials that are found in the He-shell flash convection zone. These are first of all primary ^{12}C from the triple-α He burning, possibly some ^{16}O depending on the mixing assumptions at the bottom of the He-shell flash convection zone (Herwig 2000), as well as any *s*-process elements. The nucleosynthesis and formation of the later will be described in ❯ Sect. 3.2. Whether or not, and if so at which core mass, the third dredge-up would occur was debated, since early models (e.g., Iben 1981; Vassiliadis and Wood 1993; Blöcker 1995a) did not obtain this dredge-up mixing in simulations. However, it became clear that in order to reproduce this obviously very important feature of thermal-pulse AGB calculations, some kind of nonstandard convective boundary mixing across the Schwarzschild condition (which sets the convective boundary where the adiabatic and radiative gradient are equal) was needed (Lattanzio 1986; Hollowell and Iben 1988; Lattanzio 1989; Frost and Lattanzio 1996; Herwig et al. 1997; Mowlavi 1999; Herwig 2000). This issue is now settled, and all contemporary simulations obtain amounts of third dredge-up that are broadly consistent with observational constraints.

Such constraints come from a combination of observations. In particular, the synthetic models by Marigo et al. (1996, and subsequent work) that initially incorporated the third dredge-up as a free parameter have been tremendously useful to establish when and how efficiently the third dredge-up has to operate. Constraints include the luminosity function of C stars (Marigo et al. 1999), the star counts of O- and C-rich stars in clusters or extragalactic populations, the observed abundance of AGB stars (e.g., Fig. 6 in Herwig 2005), planetary nebulae and post-AGB stars, as well as additional constraints from nucleosynthesis discussed in ❯ Sect. 3.2.

The efficiency of the third dredge-up will also depend on nuclear physics input. For example, the downward revision of the ^{14}N$(p, \gamma)^{15}$O rate leads to weaker H-shell burning, larger peak He-shell flash luminosities, and more efficient third dredge-up (Herwig and Austin 2004; Herwig et al. 2006a).

Nonstandard mixing during and at the end of the third dredge-up is also required for the formation of a layer enriched in ^{13}C which serves as the neutron source for the *s* process, to be further discussed in ❯ Sect. 3.2. It has been proposed that convective boundary mixing needs to be taken into account as well at other convective boundaries, as, for example, at the bottom of the He-shell flash convection zone (Herwig et al. 1997; Herwig 2000; Miller Bertolami et al. 2006; Weiss and Ferguson 2009). Such mixing would have wide ranging implications for the thermal-pulse strength, the dredge-up efficiency, the *s* process in the He-shell flash convection zone, and the subsequent radiative ^{13}C-driven *s* process. Such mixing leads to larger ^{12}C and ^{16}O abundances in the intershell, in agreement with observations of H-deficient post-AGB stars (Werner and Herwig 2006). If correct, this would imply that AGB stars would dredge-up primary ^{16}O and, possibly limited to lower metallicity environments, may be a contributor of ^{16}O to the galactic chemical evolution. This type of mixing may also imply larger peak temperatures for the ^{22}Ne-fuelled *s*-process contribution. Lugaro et al. (2003) have argued that this may lead to isotopic ratio predictions, for example, for Zr, that could be incompatible with observations from presolar grains. This question needs to be revisited, considering possible modifications to the details of the mixing algorithm as well as the latest nuclear reaction rate data, in particular for the ^{22}Ne$(\alpha, n)^{25}$Mg neutron source reaction. Eventually, highly resolved hydrodynamic simulations of the He-shell flash convection may settle this question (for early attempts, see Herwig et al. 2006b, 2007).

Returning to ❯ *Fig. 8-11*, eventually the thermonuclear runaway will be quenched, and after the peak luminosity has passed, the He shell will settle for a while into a stable burning mode. The star is for a couple 1,000 yr a He-burner, and He burning takes place radiatively. While during the thermal pulse He burning is dominated by the triple-α process, the ^{12}C$(\alpha, \gamma)^{16}$O reaction dominates the radiative He burning (cf. $m_r \sim 0.6\,M_\odot$ in ❯ *Fig. 8-14* where the ^{16}O abundance exceeds the ^{12}C abundance). After the He-shell flash, the layers above the H shell, the intershell region, and the region of the H-free core contract again, and the temperature rises. As much as H-shell burning is rejuvenated, the He burning burning decreases. Finally, about 8,000–10,000 yr into the new interpulse period the AGB star is back in the H-shell-supported single-shell burning mode, and the cycle starts over again.

Remarkably, despite the enormous peak He-shell flash luminosity released into the stellar interior during a thermal pulse, the effect on the surface parameters is not too dramatic (❯ *Fig. 8-11*). Newer models with third dredge-up show the radius peak triggered by the thermal pulse. This may be relevant for binary evolution considerations. A radius peak may trigger a common envelope evolution to occur preferentially at thermal-pulse cycle phase zero, that is, immediately following the thermal pulse.

Molecules, Dust, and Grains

One of the most important results of the third dredge-up is the enrichment of the envelope and surface with the nuclear products of nuclear shell burning. The evolution of the C/O ratio (❯ *Fig. 8-12*) is important for the chemistry of molecular opacities at the surface, which in turn effects the temperature and the mass loss conditions discussed above. The chemistry at the surface will also determine the type of dust that can form. Molecular and dust chemistry are fundamentally different in C- and O-rich environments. The reason is the high dissociation energy (11.1 eV) of carbon monoxide. Thus, coming out of the star, the gas will first form CO until all of either O (in a C-rich environment) or C (if C/O < 1) is consumed (Gustafsson and Höfner 2003). On the surface of C-stars, only molecules without O can form, for example, CN, which
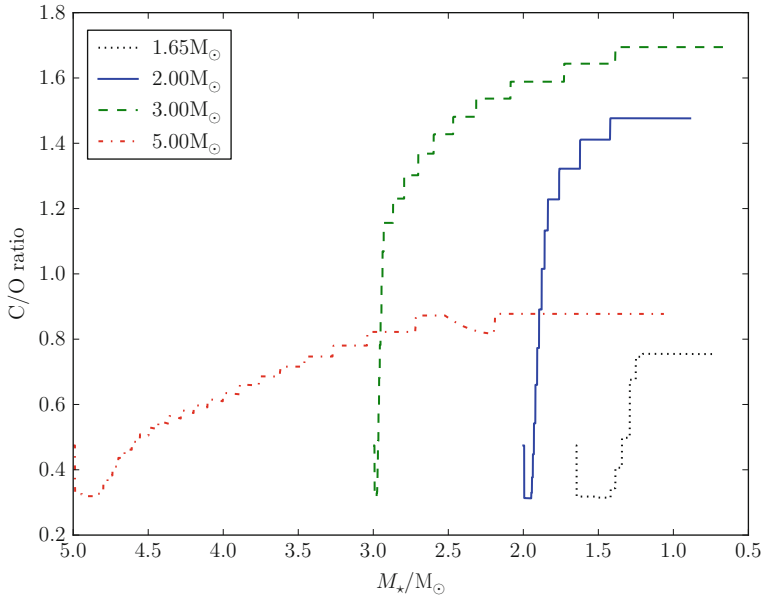
◼ Fig. 8-12

Evolution of the C/O ratio (by number) as a function of stellar mass. Since the stellar mass decreases with time the C/O evolution corresponds to a time, sequence from *left* to *right*

has been identified as a particularly important source of opacity (see above and ❯ Sect. 2). This dichotomy in chemistry between first the O-rich and later the C-rich thermal-pulse evolution is responsible for the difference in mass loss efficiency discussed above.

The evolution of the C/O ratio by number is shown in ❯ *Fig. 8-12*. The 3 $M_\odot$ case shows that the C/O ratio is increasing initially almost at constant stellar mass, reflecting the fact that during the O-rich phase of the evolution, the mass loss is smaller than in the following C-rich phase. According to the assumptions made for this calculation, the mass starts to decrease significantly only after a certain C excess has been reached. Still, further thermal pulses trigger dredge-up events that further increases the C/O ratio. However, since not too many thermal pulses can occur once the star is C-rich (because of the higher mass loss, see discussion above), there is naturally a limit on the maximum C/O ratio that can be obtained. (This limit also comes from the C/O ratio in the He-shell flash convection, which in turn depends on the boundary mixing assumptions at the bottom of the He-shell flash convection zone; see discussion in previous section on He-shell flash mixing.)

The transformation into a C-rich, high-mass loss star has another intriguing consequence, the formation of C-rich dust grains, the SiC grains. These are among the most abundant presolar grains that are extracted from meteorites (Zinner 1998). Presolar grains have formed in the cool and dense outflows of individual stars. They survived the condition in the interstellar medium until they were included unhomogenized into meteoritic material as part of the solar system formation. These grains are analyzed with great precision in the laboratory. They carry the signature of the particular nucleosynthetic processes inside individual AGB stars (or other sources,

depending on where they formed). This still young field is covered in the monograph *Stardust from meteorites. An introduction to presolar grains* by Lugaro (2005). It provides fascinating constraints on the nucleosynthesis processes in AGB stars, which will be covered next.

3.2.2 Nucleosynthesis

The events through the He-shell flash are described here once more, starting again with the quiescent H-shell burning before the 12th thermal pulse (❯ *Fig. 8-10*), however, now focusing on the nucleosynthesis. As the H shell burns through unprocessed material, it leaves behind its burning products (❯ *Fig. 8-13*). These are of course He, to be accreted by the He shell, but also, like during H-core and H-shell burning during the pre-AGB phase, most of the C and O isotopes will be transformed into ^{14}N (see discussion in ❯ Sect. 3.1). While before only the C and O from the initial composition could be transformed to ^{14}N, now also the primary C (and possibly O, see discussion in section He-flash mixing) from previous He-shell flashes, that was mixed into the envelope due to the third dredge-up, can be turned into ^{14}N. As discussed below, this is important for the *s* process.

The profiles over a larger mass range are shown in ❯ *Fig. 8-14*. The left side of the figure shows the upper parts of the CO core. The He shell is located around 0.605–0.615 M$_\odot$. The first flat profile between 0.615 and 0.622 M$_\odot$ contains the layer formally well mixed by the previous He-shell flash convection zone. The He-rich layer above, (0.623–0.627 M$_\odot$) contains the ashes
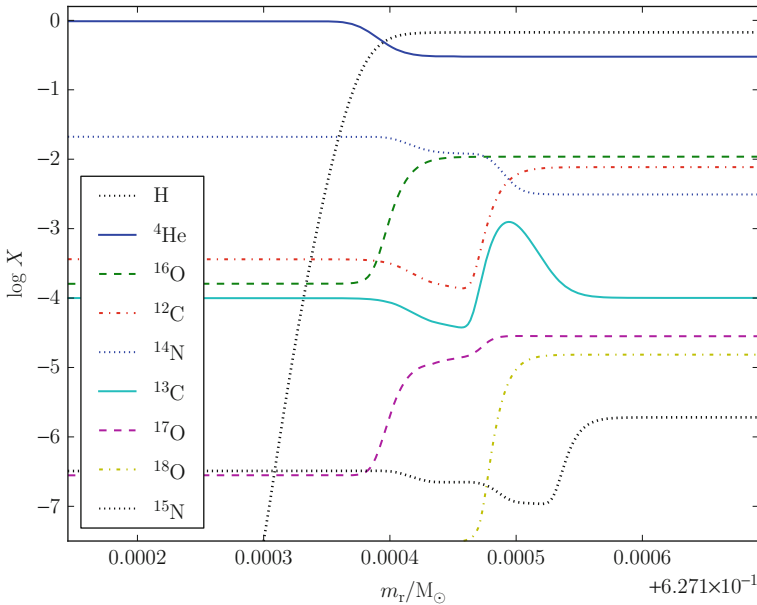
■ **Fig. 8-13**
Profiles of H, ^{4}He and the CNO isotopes in the H-burning shell during the interpulse period at time t = 41,011 yr on the time scale of ❯ *Fig. 8-10*. The order of species in the legend corresponds to the abundance of the species at the right edge of the diagram, from *top* to *bottom*
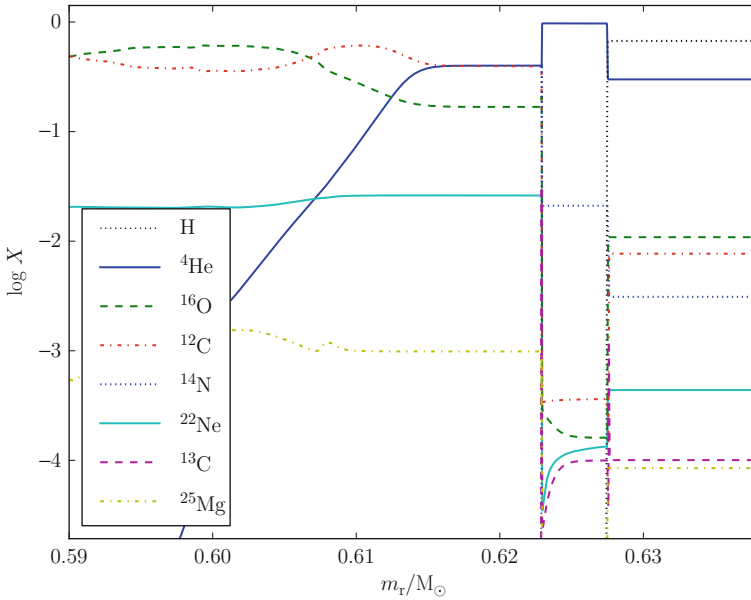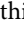
◼ Fig. 8-14

Profiles of key species from the CO core through the intershell region and the H-shell burning ashes and to the bottom of the convective envelope. As in ❯ *Fig. 8-13*, the point in time of this profile is *t* = 41,011 yr on the time scale of ❯ *Fig. 8-10*. The mass range is the same as in the Kippenhahn diagram ❯*Fig. 8-10*. The order of species in the legend corresponds to the abundance of the species at the right edge of the diagram, from *top* to *bottom*

of the H-shell burning during the present interpulse phase, and above the abundance profile of the bottom layers of the convective envelope can be seen. The variation of the ^{12}C/^{16}O ratio has already been pointed out, and it is a signature of the T dependence of the ratio of the triple-α to ^{12}C$(\alpha, \gamma)^{16}$O rate.

Neutron Sources for the *s* Process

Another important feature of this diagram (❯ *Fig. 8-14*) is the significant enhancement of the ^{22}Ne and ^{25}Mg abundance in the intershell region. Because the thermal pulses discussed here have a dredge-up parameter $\lambda \sim 1$ (see above), the abundance profiles after the following thermal pulse would look almost identical. The high ^{22}Ne and ^{25}Mg abundance are the result of the nucleosynthesis in the He-shell flash convection zone. The large amount of primary ^{14}N in the H-burning ashes is completely mixed into the next He-shell flash convection zone (cf. ❯ *Fig. 8-10*) where it is burned into ^{22}Ne by the same chain of two α capture already discussed in ❯ Sect. 3.1. In stars as massive as this 3 M$_\odot$ case, the peak temperature at the bottom of the He-shell flash convection zone is high enough to activate the reaction ^{22}Ne$(\alpha, n)^{25}$Mg. This reaction is one of the two main neutron source reactions, and it leads to *s*-process nucleosynthesis in the He-shell flash convection zone that will be discussed below. The ^{25}Mg is only a tracer of that reaction, and the elevated abundance in the intershell indicates that neutrons have been released here during previous cycles.

But there is another and even more important neutron source in the thermal-pulse AGB stars, as discovered by Straniero et al. (1995). This neutron source is the $^{13}C(\alpha, n)^{16}O$ reaction. However, in standard stellar evolution models, there is no appreciable source of ^{13}C, unlike the situation for ^{22}Ne which, as already mentioned, forms quite naturally even in a primary manner out of the ^{14}N from the ashes of the H shell that burns through third dredge-up C and O enriched envelope material. Therefore, it is assumed that additional mixing processes, beyond what the mixing-length theory and the Schwarzschild condition account for, must be at work. If the location of these additional mixing processes is the bottom boundary of the convective envelope during the third dredge-up (time marker 1,300 yr, m_r = 0.622 M$_\odot$, ❷ *Fig. 8-10*, left panel), and if it mixes a sufficient amount of H from the envelope into the ^{12}C-rich intershell, then everything else will fall in place. The necessity to have some mixing at that convective boundary was already mentioned in the context of obtaining the third dredge-up (see above), and here such mixing is also needed.
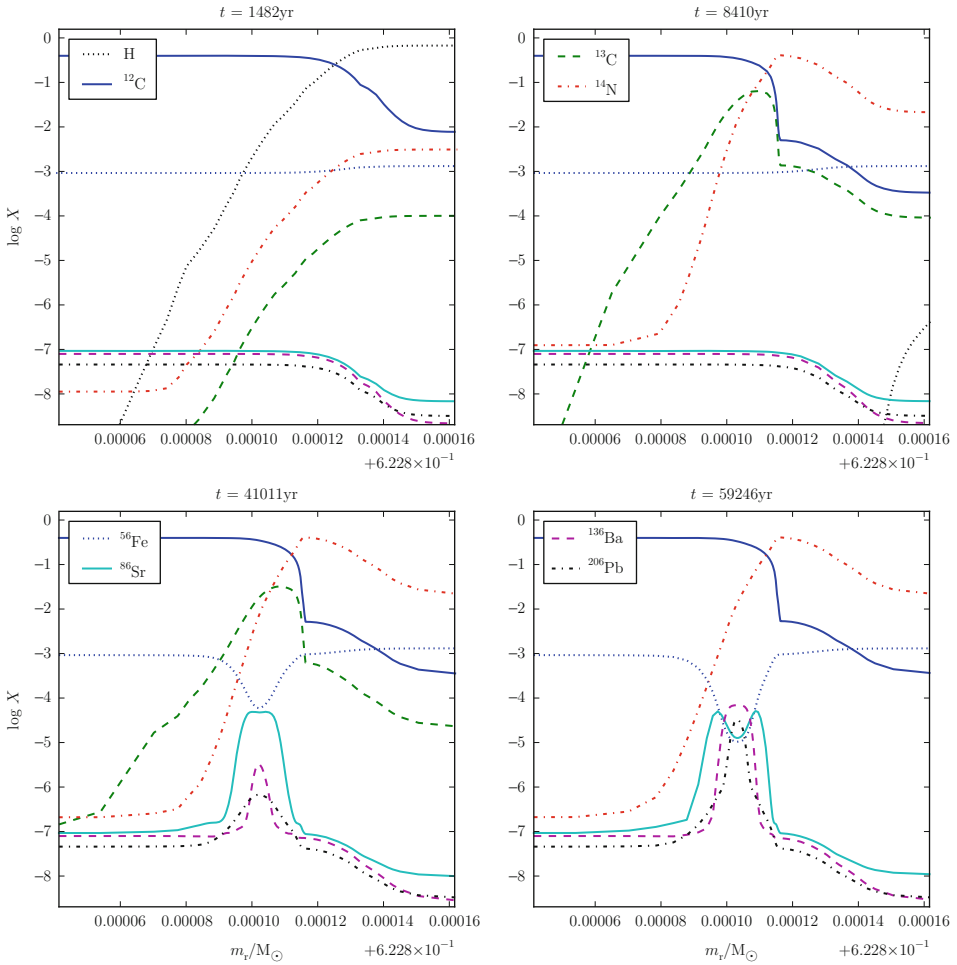
The ^{13}C Pocket

The models discussed here include a simple model for convective boundary mixing that was first introduced in stellar evolution models by Herwig et al. (1997). After the diffusion coefficient D is calculated inside the convectively unstable zone from the mixing-length theory, the diffusion coefficient for mixing is extended into the formally stable layer by an exponentially decreasing function of the distance from the formal convective boundary:

$$D_{OV} = D_0 \exp\left(-\frac{2|r - r_0|}{f H_P}\right) \tag{8.8}$$

where H_P is the pressure scale height and D_0 is the mixing-length diffusion coefficient, both taken at the radius r_0 close to the boundary. In this model, f is a free parameter that has to be calibrated for each type of convective boundary either semiempirically through observations or through hydrodynamic simulations. Lugaro et al. (2003) have used this framework with f = 0.128 to generate a mixing zone that is of the required order of magnitude size to reproduce observed overabundance levels of s-process enriched AGB stars (see also Herwig et al. 2003). A more in-depth discussion of the partial-mixing zone has been given by Straniero et al. (2009) with applications in Cristallo et al. (2011).

The formation of the partial-mixing zone during the dredge-up due to the mixing model (❷ 8.8), and the subsequent nucleosynthesis in the ^{13}C-pocket is illustrated in ❷ *Fig. 8-15*. The top-left panel shows the formation of the partially mixed layer across the bottom boundary of the envelope convection zone shortly after that boundary has reached the smallest mass coordinate at the end of the third dredge-up phase. The mixing model forces protons below the Schwarzschild boundary, and as a result, the abundances are transitioning smoothly at the envelope–core interface over a mass region with width $\Delta M_{PM} \sim 2 - 3 \times 10^{-5}$ M$_\odot$ (which is probably a bit smaller than what is required to reproduce observed s-process overabundances quantitatively). The width of this partial-mixing layer, of course, is the direct consequence of the choice of f in ❷ 8.8.

Once contraction resumes after the He-shell flash (see discussion above), the temperature in the partial-mixing zone gradually increases (Fig. 6, Herwig et al. 1999) and H burning resumes by creating a pocket of ^{13}C and ^{14}N (upper-right panel, note the tail of the H profile at the very right end of the plot). Then, for a long time, nothing happens, until the temperature reaches $T \sim 10^9$ K to activate the $^{13}C(\alpha, n)^{16}O$ reaction. Peak neutron densities around $N_n \sim 10^7$ cm^{-3}

◨ Fig. 8-15

Profiles of key species showing the formation and evolution of the ^{13}C-pocket during the interpulse phase, the primary site of the main *s* process. The times of the four frames correspond to the time scale of ❯ *Fig. 8-10*. The mass range is zoomed in around the envelope–core interface at the end of the third dredge-up (*upper-left panel*) when a simple mixing model generates a partial-mixing zone containing both H and ^{12}C. A few thousand years later, ^{13}C has formed (*top-right panel*), and again, a few ten thousand years later, neutrons are released, and copious amounts of trans-iron elements form (*bottom-left*), leading eventually to the formation of Pb (*bottom-right panel*). Fe is the seed for the *s* process

are maintained for several 1,000 up to 10^4 yr, and the neutron exposure is $\tau \sim 0.2 - 0.4$ mbarn^{-1}. In simulations with a partial-mixing model the peak neutron exposure is proportional to the intershell ^{12}C abundance, which in turn is proportional to the mixing efficiency at the convective

bottom boundary of the He-shell flash convection zone (Herwig et al. 1999; Lugaro et al. 2003; Herwig 2005). The neutrons are captured by ^{56}Fe and trans-iron elements form.

The *s*-process abundance distribution is characterized by three distinct peaks corresponding to the low *n*-capture cross sections at the neutron magic-number closed shells at *n* = 50, 82, and 126. In the lower-left panel, ^{86}Sr, representing the first *s*-process peak, increases first as the nuclear production through continued neutron captures on seed nuclei arrives at the *N* = 50 barrier. The second peak elements, represented by ^{136}Ba are at this point enhanced much less, and the third peak species, represented by ^{206}Pb are only starting to be produced. The *s*-process seed, ^{56}Fe is significantly depleted in the ^{13}C pocket.

The final panel (bottom right) shows the situation immediately before the nuclear products will be mixed into the next He-shell flash convection zone. Now, the ^{86}Sr profile itself has a little dip in its peak, because it has served as a seed for higher mass species. The network flux has reached now Pb, and species of all three *s*-process peaks are enhanced by approximately the same amount, that is, almost 3 dex compared to the already enriched intershell abundance of trans-iron elements as a result of previous thermal-pulse cycles and $\gtrsim$4 dex compared to the envelope abundance of the *s*-process elements (at the first thermal pulse, the intershell abundance would have a level less than the present envelope abundance). This is the result of the radiative *s* process driven by the ^{13}C pocket.
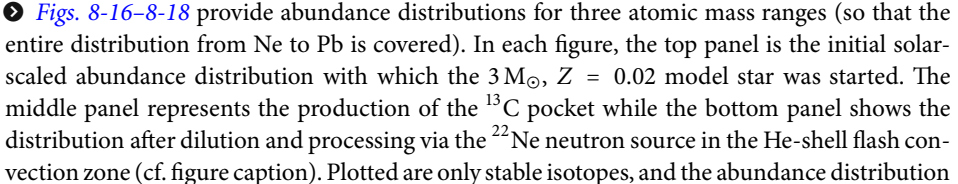
When mixed into the He-shell flash convection zone, the content of the ^{13}C pocket will first be diluted with the ratio of the mass in the partial-mixing layer to the mass in the He-shell flash convection zone $\Delta M_{PM}/\Delta M_{HeCZ} = 2.1 \times 10^{-5}/0.021 = 1/1,000$. Then, the freshly produced heavy elements, mixed with the heavy elements already present from previous thermal pulses will be exposed to the ^{22}Ne neutron source, the origin of which was described above. Although the He-shell flash convection lasts for about 150 yr (see discussion above), the temperature is only for a short fraction high enough (log *T* > 2.7) to activate the ^{22}Ne$(\alpha, n)^{25}$Mg neutron source. Again, depending on the convective boundary mixing assumptions, and on the core mass, the duration of the high-T phase varies from less than 1 yr to a few years, and the peak neutron density reaches $N_n \sim 10^9 - 10^{11}$ cm^{-3} which implies neutron exposures in the range $\tau \sim 0.01 - 0.90$ mbarn^{-1}. Presently, models with larger convective boundary mixing predict higher peak temperatures, longer high-T periods, and consequently higher neutron densities. Lugaro et al. (2003) have pointed out that such models may be incompatible with measurements of isotopic ratios, for example, the ^{96}Zr/^{94}Zr ratio, in presolar grains, which are sensitive to *s*-process branchings, in this case at ^{95}Zr. Clearly, these issues need further investigations, but the interconnections between the details of the *s* process with aspects of the dynamical star (❯ Sect. 5) are intriguing.
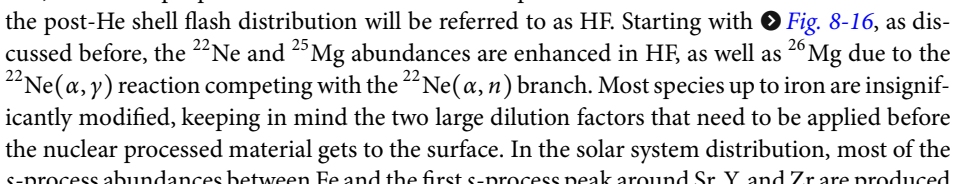
After the end of the exposure in the He-shell flash convection zone, the *s*-process enriched material will be mixed into the envelope, again with a large dilution factor $\Delta M/M_{env}$ (see discussion in section *He-shell Flash Mixing and Third Dredge-Up* ❯ Sect. 3.2.1).

The present generation of models, such as those illustrated here, or those by Cristallo et al. (2011), include the mixing processes into the stellar evolution code, and at least any feedback that such mixing may have back to the stellar structure would be taken into account. An example for such feedback can be encountered in simulations of stars with very-low metallicity, where the mixing of protons into the ^{12}C-rich intershell leads to a hot dredge-up (Goriely and Siess 2004; Herwig 2004) with poorly understood quantitative consequences for the nuclear yield predictions and final stellar evolution outcomes. In any case, the properties and realistic modeling of the mixing for the ^{13}C pocket remains an open problem.

s-Process Nucleosynthesis

Much of what is known today about the s process quantitatively has been discovered through a parameterized post-processing method, in which the required amount of ^{13}C was directly inserted into the post-processing calculation. This approach was pioneered by Gallino et al. (1998), and follow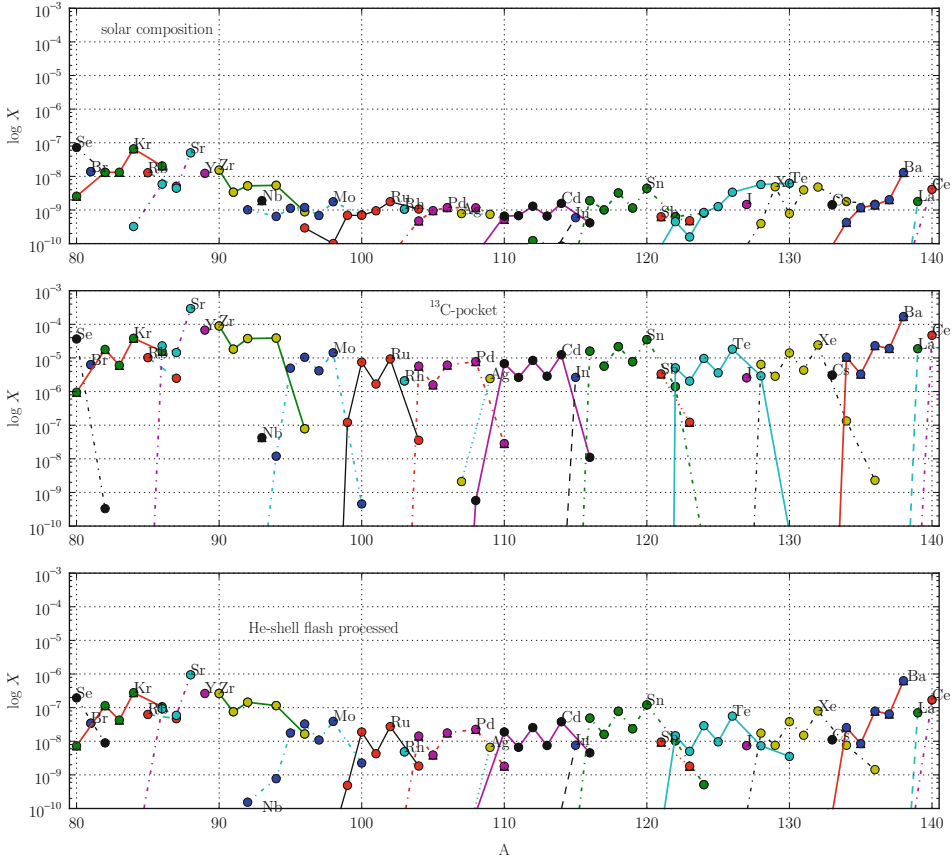ed by many others, including Busso et al. (2001), and Travaglio et al. (2004) with a focus on galactic chemical evolution, and Bisterzo et al. (2010) with an emphasis on low-metallicity stars. Käppeler et al. (1989) and Busso et al. (1999), and more recently Käppeler et al. (2011) provide a detailed discussion not only on simulation results but also on the nuclear physics involved (incl. discussions on s-process branchings) and on comparisons with and constraints from observations.

Here it is not the intention to give a comprehensive overview of the results covered in an extensive body of literature (see above for examples). Instead, some features of the workings of the s process are highlighted which may help to understand that body of literature better. ❯ *Figs. 8-16–8-18* provide abundance distributions for three atomic mass ranges (so that the entire distribution from Ne to Pb is covered). In each figure, the top panel is the initial solar-scaled abundance distribution with which the $3\,M_\odot$, $Z = 0.02$ model star was started. The middle panel represents the production of the ^{13}C pocket while the bottom panel shows the distribution after dilution and processing via the ^{22}Ne neutron source in the He-shell flash convection zone (cf. figure caption). Plotted are only stable isotopes, and the abundance distribution has not been decayed. Careful inspection of these plots reveals a number of interesting aspects about the different components of the heavy element nucleosynthesis, in fact more than can be discussed here. The abundances in these diagrams are the result of theoretical stellar simulations and of the nuclear physics network of isotopes and rates used. Therefore, limitations in our present understanding on stellar physics and nuclear physics may affect the accuracy of such predictions. For instance, final abundances at branching points located along the s-process path are very sensitive to the uncertainties of the nuclear rates involved. Furthermore, the treatment of ground and isomeric states of isotopes that are not fully thermalized at stellar conditions is still not clear (e.g., Kr85 is a branching point in the s-process path, and its ground and isomeric state are not thermalized at typical s-process conditions in low-mass AGB stars and should therefore be treated separately, e.g., Ward and Fowler 1980).

Just for the purpose of this discussion, the ^{13}C pocket frame will be referred to as CP, and the post-He shell flash distribution will be referred to as HF. Starting with ❯ *Fig. 8-16*, as discussed before, the ^{22}Ne and ^{25}Mg abundances are enhanced in HF, as well as ^{26}Mg due to the ^{22}Ne(α, γ) reaction competing with the ^{22}Ne(α, n) branch. Most species up to iron are insignificantly modified, keeping in mind the two large dilution factors that need to be applied before the nuclear processed material gets to the surface. In the solar system distribution, most of the s-process abundances between Fe and the first s-process peak around Sr, Y, and Zr are produced by the weak s process in massive stars, where a nonnegligible contribution is also supposed to come from AGB stars, in particular from massive AGB stars.

Skipping therefore right through to the first peak isotopes, ^{84}Sr is a p-process element which cannot be reached by neutron captures in the s process. It is therefore only destroyed in CP and HF. However, the other three Sr isotopes show in both panels the same relative ratios as in the solar distribution. The same is true for the ratios of ^{88}Sr, ^{89}Y, and ^{90}Zr, indicating their dominantly s-process origin. For Zr, the solar isotopic ratios for the mass numbers 90, 91, and 92 are well reproduced by CP. However, ^{96}Zr is produced ~2 dex less in CP compared to the solar-scaled distribution. The reason for that is the branching at ^{95}Zr where the β decay with a terrestrial half life of 64d competes with a neutron capture. In the ^{13}C pocket, the neutron

◨ Fig. 8-16

Abundance distribution (mass fraction) for the solar composition (*top panel*) and in comparison the abundance distribution averaged over the ¹³C pocket at the end of the interpulse (*bottom-right panel*, ⊙ *Fig. 8-15*), just before its nuclear production will be engulfed into the next He-shell flash convection zone (see ⊙ *Fig. 8-10*, *t* = 59,246 yr), and finally averaged over the mass region of the He-shell flash convection zone, after the pulse is finished. The *bottom panel* therefore shows the abundance distribution in the intershell region, part of which will be mixed to the envelope during the immediately following third dredge-up. The atomic mass ranges from the light elements that are not significantly effected by the *s* process through Fe which is the seed of the *s* process to just past the first *s*-process peak around Sr, Y, and Zr

density is too low to open the branching and all ^{95}Zr will decay to ^{95}Mo. However, as the HF panel shows, in the high neutron density environment of the He-shell flash convection zone, at least in the 3 M$_\odot$ case considered here, the branching is in fact open, and ^{96}Zr is produced. In fact, after processing in the HF, the ratios of all the Zr isotopes seem to reproduce the solar ratios.

Zr is an example that demonstrates how the bulk of the *s*-process production takes place in the ^{13}C pocket, while certain isotopic rearrangements are taken care of by the ^{22}Ne neutron source in the He-shell flash convection zone. The sensitivity of such branchings to the exact
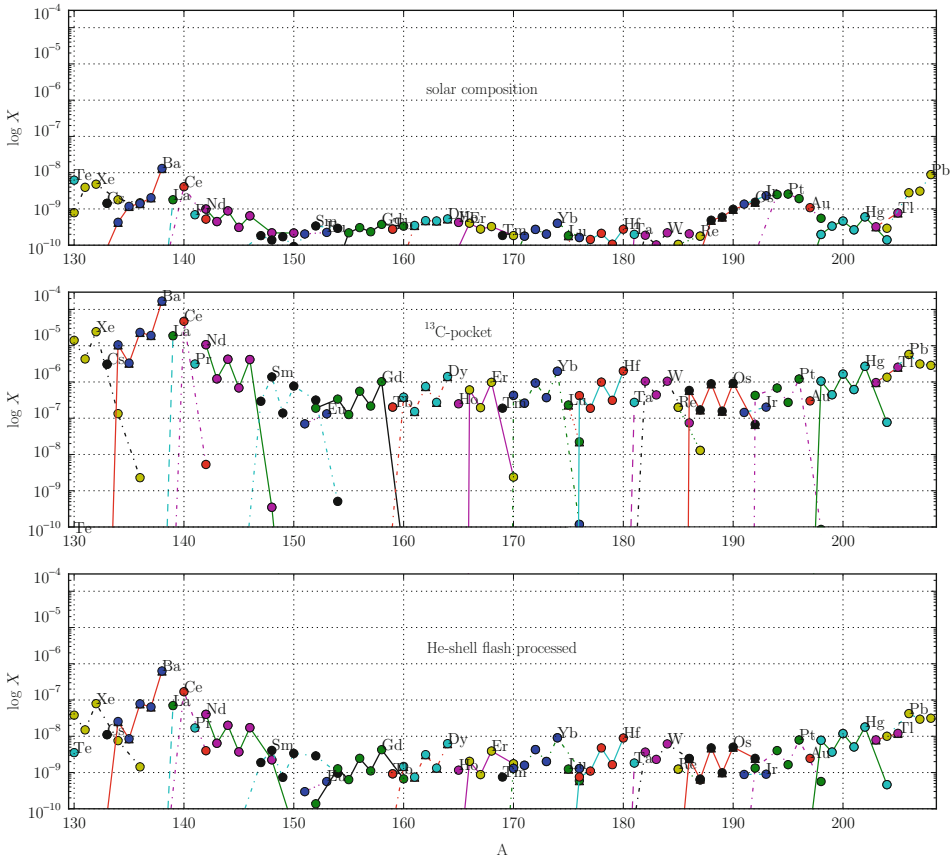
◼ Fig. 8-17
Same as ❯ Fig. 8-16, for the atomic mass range from the first s-process peak to past the second s-process peak around Ba and La

details of the thermodynamic and hydrodynamic conditions in the convection zone may provide eventually a powerful diagnostic tool for constraining mixing physics, given that other physics ingredients, such as the nuclear physics, are known to sufficient accuracy.

In this discussion, the main emphasis is on s-process signatures in the solar-scaled initial abundance distribution. However, only about half of all trans-iron elements are made in the s process (Arlandini et al. 1999). The other half comes from the r process, and it should be expected that there are numerous patterns that are not the result of the nucleosynthesis in $3\,M_\odot$ stars. In addition, the solar abundance distribution is the superposition of many sources as a result of galactic chemical evolution, including s-process production from a range of initial masses.

The r process is taking place in some kind of explosive environment in which very large neutron densities ($N_n \gtrsim 10^{20}\,\mathrm{cm}^{-3}$) can be reached (Meyer 1994; Sneden et al. 2008). Sites that have been suggested for the r process include neutron-star mergers (Freiburghaus et al. 1999) or supernova fallback (Fryer et al. 2006). Simplified, in the r process the very large neutron

◧ Fig. 8-18

Same as ❯ Fig. 8-16, for the atomic mass range from the second s-process peak to Pb

densities first drive the network flux out to the neutron drip line from where nuclei decay back to the valley of stability.

Moving on to ❯ Fig. 8-17, [101]Ru and [104]Ru are not produced either in CP or sufficiently in HF. Both of these are predominantly produced by the *r* process. This is an example of how a pronounced odd-even effect from the s process in one stellar model will be complemented by other sources and processes. Such aspects of galactic chemical evolution have been addressed, for example, by Timmes et al. (1995) and Travaglio et al. (2004).

Sn is another example that seems to be well reproduced by the *s*-process prediction from mass number 116 to 121. Again, [112]Sn is a *p*-process isotope, while [124]Sn would come from the *r* process. Similar arguments would indicate that [122]Te, [123]Te, and [124]Te are primarily produced by *s* process. In fact, these are *s*-only isotopes which are shielded by stable species on the same isobar on the neutron-rich side. Therefore, they cannot be produced by the *r* process. However, this is not the case for the more massive Te isotopes, and their production is dominated by the *r* process. It is interesting to note though that some although insignificant amount of [130]Te is produced in HF, indicating again some branching activity. Also, for Xe and Ba, the ratio of

the *s*-only isotopes in the solar abundance distribution is well reproduced in CP and HF. For completeness, the corresponding plot for the mass range between the second and the third peak is provided (❯ *Fig. 8-18*). It reveals upon inspection, aided by a chart of nuclei (http://www.nndc.bnl.gov/chart) similar details about the production mode of each isotope.

3.2.3 Post-AGB Evolution

Once the AGB star has lost all but a small fraction of the original envelope, the star will evolve away from the giant solution, initially on a thermal time scale, at constant luminosity to high temperatures. The unprocessed envelope mass that is left on the surface depends on the core mass and is a result of stellar evolution simulations of this transition phase. The envelope mass is approximately $10^{-4}\,\mathrm{M_\odot}$ for a core mass of ~0.6 $\mathrm{M_\odot}$. For the massive cores, this will decrease by approximately an order of magnitude while the less massive He-white dwarfs will have envelope masses larger than $10^{-3}\,\mathrm{M_\odot}$ (Schönberner 1981; Driebe et al. 1998).

The post-AGB evolution is shown for three stellar evolution tracks with masses around $1\,\mathrm{M_\odot}$ as part of an HRD diagram showing the entire evolution from main sequence to white dwarf, in ❯ *Fig. 8-19*.

The horizontal evolution from cool to hot at constant luminosity corresponds to the decrease of the envelope mass due to mass loss and due to nuclear burning. In fact, the temperature of the star along the constant luminosity cooling track is directly correlated with the envelope. The luminosity follows the core-mass luminosity relationship (❯ Sect. 3.2.1) and is
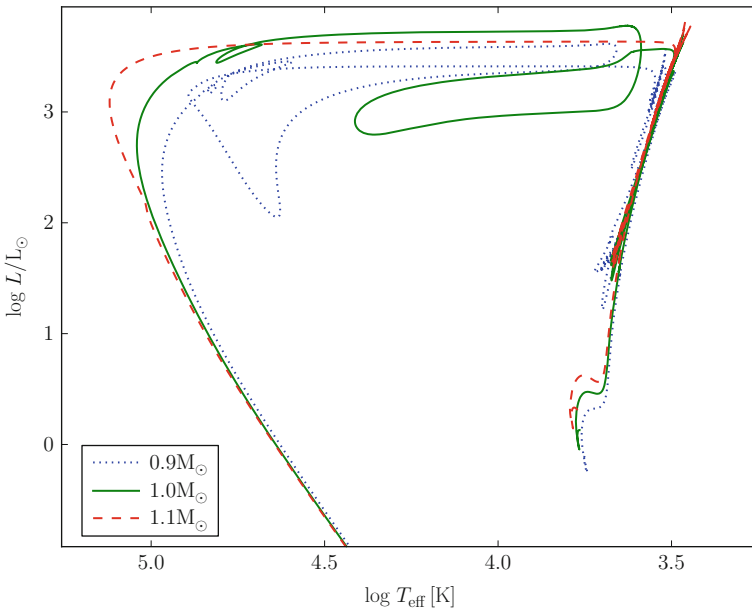
◼ **Fig. 8-19**
HRD for stars with masses around $1\,\mathrm{M_\odot}$ and Z = 0.01, including the post-AGB and white dwarf evolution. The white dwarf masses are M_f = 0.525, 0.543, and 0.554 $\mathrm{M_\odot}$ for M_{ZAMS} = 0.9, 1.0, and 1.1 $\mathrm{M_\odot}$. The 0.9 $\mathrm{M_\odot}$ track arrives on the white dwarf cooling-down track after 1.47×10^{10} yr

therefore set. For a $1\,M_\odot$ post-AGB star (which would have started its evolution with M_{ZAMS} $\sim 6\,M_\odot$, see ❯ *Fig. 8-21*), one may expect a nuclear burning rate of $\dot{M}_{H-shell} \sim 4 \times 10^{-7}\,M_\odot/yr$ while a star with $0.65\,M_\odot$ will have a lower burning rate of $\sim 1.4 \times 10^{-7}\,M_\odot/yr$.

Mass Loss

The time scale on which the post-AGB star evolves to the hottest point may depend therefore on the mass loss, if it is larger than $\dot{M}_{H-burn}$. Higher mass loss implies a shorter post-AGB evolution time scale (Schönberner 1981; Blöcker 1995b). AGB mass loss decreases steeply with increasing stellar temperature because dust formation is less efficient at higher temperature, and because the material at the surface is gravitationally more bound when the radius is smaller (and the escape velocity is higher). For temperatures above $\sim 5,000\,K$, the mass loss according to formulae that are intended to capture the mass loss mechanism of AGB stars (Arndt et al. 1997; van Loon et al. 2005) falls below $\dot{M}_{H-burn}$. Hotter stars have radiation-driven wind mass loss $\dot{M}_{rad-wind}$ (Pauldrach et al. 1988, see also chapter on winds in this volume). For lower-mass post-AGB stars, such as the $0.65\,M_\odot$ example given above, $\dot{M}_{rad-wind} < \dot{M}_{H-burn}$. Therefore, if the wind-driven mass loss theory is correct, the post-AGB evolution time will be uniquely determined due to the mass of the post-AGB star. For higher mass cases, such as the $1.0\,M_\odot$ case, $\dot{M}_{rad-wind} \gtrsim \dot{M}_{H-burn}$, and in this case, the transition time from the AGB to the hot "knee" where the track turns around into the WD cooling track will depend on the mass loss as well.

Note that the correlation between temperature and envelope mass implies that H-deficient (or H-free) central stars of planetary nebulae of type PG 1159 or [WC] (Werner and Herwig 2006) or white dwarf of type DQ or DZ (see chapter on white dwarfs in this volume) cannot form due to enhanced mass loss that expels the remaining H-rich envelope. Such an enhanced mass loss would simply accelerate the post-AGB evolution, and the resulting envelope mass of the pre-WD remains the same. The envelope mass of white dwarfs can now be probed by asteroseismology.

Post-AGB He-Shell Flashes

Instead, the main mechanism that causes H deficiency in post-AGB stars and young white dwarfs is believed to be He-shell flashes on the post-AGB (Herwig 2001b; Werner and Herwig 2006). As discussed in ❯ Sect. 3.2, He-shell flashes occur in regular intervals. The evolution from the AGB to the post-AGB and eventually to the WD cooling track is comparable to a fraction of the order 10% of the interpulse time, depending on mass. H-shell burning will cease when the envelope mass is too low to support H-burning temperatures at the mass coordinate where the H-free core begins. At that point, the star evolves off the horizontal post-AGB track and enters the white dwarf cooling track. This hottest feature of the post-AGB evolution is also referred to as the knee.

He burning takes place in deeper layers. While the star is evolving along the post-AGB track, the thermal-pulse clock continues to tick in the He-shell region. Clearly, if the post-AGB star has evolved onto the proper WD cooling track, no nuclear process can take place anymore. However, the AGB star statistically happens to leave the giant configuration at a time in the thermal-pulse cycle before the He-shell flash that is comparable to the evolution time to the WD cooling track. In that case, the next He-shell flash will take place during the post-AGB evolution (Fujimoto 1977; Schönberner 1981; Iben et al. 1983; Iben and MacDonald 1995; Herwig et al. 1999).

Both the $0.9\,M_\odot$ and the $1.0\,M_\odot$ tracks in ❯ *Fig. 8-19* show the characteristic loops associated with post-AGB He-shell flashes, which usually cause a temporary evolution back to the AGB regime in the HRD. For this reason, this phenomenon is also called *born-again* evolution. Several born-again stars, such as Sakurai's object (e.g., Duerbeck and Benetti 1996; Hajduk et al.

2005), FG Sge (Blöcker and Schönberner 1997; Jeffery and Schönberner 2006), or V605 Aq (e.g., Clayton et al. 2007; Hinkle et al. 2008), are known.

Two cases need to be distinguished. If the He-shell flash occurs during the high-luminosity horizontal post-AGB evolution before the knee, the H-burning shell is still on. A high entropy barrier prevents the mixing of the H-rich envelope into the He-shell flash convection zone. However, the stellar surface will become H-poor later during the born-again phase due to the emerging envelope convection and mass loss. This case is also called the late thermal pulse (LTP). If the He-shell flash occurs later, after the star has evolved past the knee, the H-shell is extinct, and the He-shell flash convection zone will engulf the H-rich envelope. This is called a very-late thermal pulse (VLTP). An example of such a case is Sakurai's object (Herwig 2001a; Lawlor and MacDonald 2003). Sakurai's object has detailed surface abundance observations of trans-iron elements (Asplund et al. 1999) and can be used to guide and constrain models and simulations of the physics of H combustion, that is, the interaction of rapid nuclear energy release from the $^{12}C(p,\gamma)^{13}N$ reaction with hydrodynamic and turbulent convection flow (Herwig et al. 2011 and ❯ Sect. 5).

Very similar events are known from post-RGB evolution, where flash mixing of H from the remaining envelope into a post-RGB He-core flash has been associated with horizontal branch features in globular clusters (e.g., Brown et al. 2001).

Abundance Determinations from Post-AGB Stars

When post-AGB stars evolve along the high-L horizontal track, they evolve through a range of temperatures and can be spectroscopically observed (van Winckel 2003). As a result, detailed abundance information has been obtained, in particular of many heavy elements that have formed through the s process during the progenitor AGB evolution. The abundances of post-AGB stars represent the final enrichment of the envelope with s-process elements that have formed cumulatively over many thermal pulses. Any future generation of stellar evolution and nucleosynthesis simulations needs to be confronted with this type of data.

4   Evolution as a Function of Initial Mass

Most of the basic processes and concepts of solar and intermediate-mass stars were covered by the description of the evolution of the 3 $M_\odot$ star. This chapter covers how the evolution depends on mass and introduces some processes, like hot-bottom burning that are unique to stars of other masses.

H- and He-Core Burning

Stellar evolution times depend significantly on the initial mass. Higher mass stars evolve faster than lower mass stars, as illustrated in ❯ *Fig. 8-20*. All evolutionary phases after He-core burning are short compared to H- and He-core burning. One of the greatest sources of uncertainty concerning stellar lifetimes remains the efficiency of core overshooting. The reproduction of the observed width of the main sequence requires some convective overshooting to extend the main sequence to higher luminosities (Schaller et al. 1992). Such overshooting will prolong H-core burning lifetimes. Rotation will also broaden the main sequence. At masses below $M_{ZAMS} \sim 1.25\,M_\odot$, H-burning will be radiative. In the transition region between radiative cores
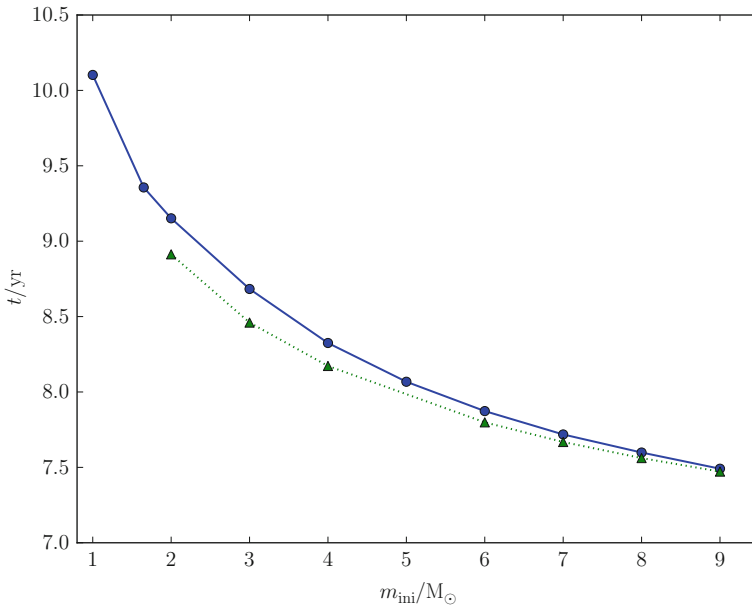
◼ Fig. 8-20
Stellar age versus initial mass for $Z = 0.02$ (*solid line* with *circles*) and $Z = 6 \times 10^{-4}$ (*dashed line* with *triangles*)

and extended convective cores, the overshooting efficiency, which is often based on parameterizations in terms of the pressure scale height at the convection boundary, needs to be carefully ramped up in order to avoid artificially enlarged convective cores (VandenBerg et al. 2006).

Lower mass stars, like the sun, will have convective envelopes during the main-sequence evolution while more massive main-sequence stars have radiative envelopes. Overlaying opacities and profiles of stars with different masses in the $\rho - T$ diagram (such as in Fig. 3 in Paxton et al. 2011) demonstrate that convective stability or instability of envelope and core regions as a function mass can be understood in terms of the variation of opacities as a result of atomic physics in terms of ρ and T, and its effect on stability via the radiative gradient (❷ 8.3).

A major source of uncertainty during He-core burning is again mixing. Here, the complicated situation of semi-convection, that was introduced in ❷ Sect. 2, implies that He-core burning lifetimes and subsequently the core masses at the first thermal pulse for a given initial mass are still uncertain. This is particularly unfortunate because the thermal-pulse AGB evolution, as, for example, the onset and efficiency of the third dredge-up does depend sensitively on the core mass.

The Initial–Final Mass Relation
The initial–final mass relation relates the initial, main-sequence mass with the mass of the white dwarf that is the evolutionary end point of solar and intermediate-mass stars (Weidemann 2000). Observational constraints seem to indicate a significant spread in WD masses for a given initial mass (Catalán et al. 2008). Several processes could be responsible for that, including WD

mergers or other binary interactions, or differential mass loss, for example, as a result of stellar rotation.

The importance of this relation derives from the fact that it relates two other important relations: the initial mass function (Kroupa 2002) and the white dwarf mass distribution (e.g., Liebert et al. 2005). Ignoring the effect of ongoing star formation, the initial–final mass relation maps the initial mass function to the white dwarf mass distribution. An initial-final mass relationship that creates a consistent picture between the IMF and the white-dwarf mass distribution is a powerful constraint on evolution simulations of solar and intermediate-mass stars.

A theoretical initial–final mass relation is shown in ❯ *Fig. 8-21* for three metallicities. According to the initial mass function, most stars (≳85%) have low-mass ≲2.5 $M_\odot$. The white dwarf mass distribution is sharply peaked around 0.59 $M_\odot$. That means that stars with initially around or below 2.5 $M_\odot$ have to be projected by the MiMf relation to the WD mass distribution peak. Such considerations have been performed quantitatively by Ferrario et al. (2005). They find the best fit to the white dwarf mass distribution with an MiMf relation with double curvature shown in ❯ *Fig. 8-21* for comparison. The MiMf relation is in this way an important global
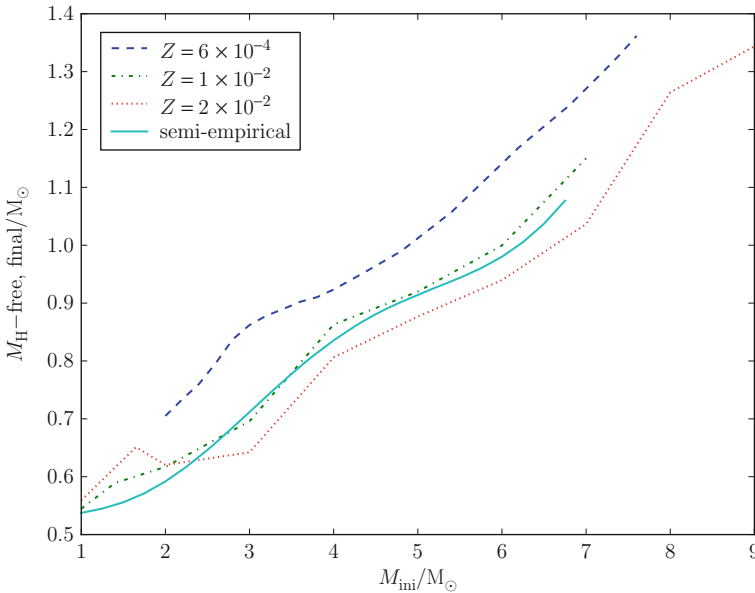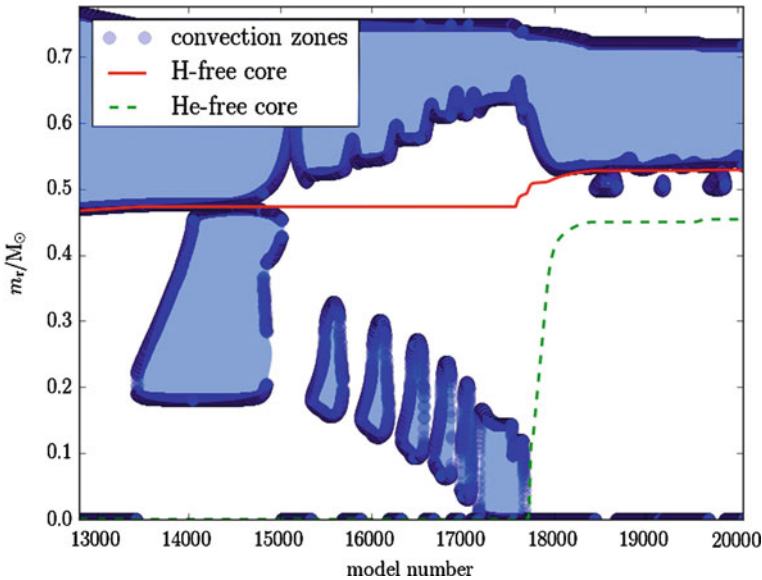

■ **Fig. 8-21**
H-free core mass at the last computed thermal pulse as a function of initial mass. Each relation is based on a grid of sequences that have been computed to the tip of the AGB when all mass is lost or close enough to the point that very little change of the core mass is expected before the model stars evolve to become white dwarfs. Therefore, the shown relations constitute theoretical initial to final mass relations for the given metallicities. The *line* **with the label** *semiempirical* **represents the curvature MiMf that Ferrario et al. (2005) found to best reproduce the white dwarf mass distribution from the Palomar-Green survey**

constraint on the evolution models. The lower mass models cannot have a lot of core growth, with implications for mass loss and third dredge-up efficiency.

**Low-Mass Stars with He-Core Flash and Those Which Become C-Rich AGB Stars**

Some of the structure in the MiMf relation may be related to initial mass limits of different burning types. Stars with $M_{ZAMS} \lesssim 1.5\,M_\odot$ will ignite He-core burning under degenerate conditions (Serenelli and Weiss 2005). The characteristic triangle-shaped feature of the $1.65\,M_\odot$ track in the $\rho_c - T_c$ (❯ *Fig. 8-3*) signals the expansion of the core at constant degeneracy (parallel to the $P_{gas} = P_{deg}$ line) has a result of the energy input from the flash, followed by heating at almost constant pressure (sharp upward evolution at $\log \rho_c \sim 4.5$) toward the location of He-core burning. A Kippenhahn diagram of a stellar evolution simulation through the He-core flash is shown in ❯ *Fig. 8-22*. Using the model number instead of time on the abscissa allows to show both the short-lived He-core flash, followed by multiple smaller post-flashes, the He-core burning (model ~17,100–17,900), the early AGB evolution, as well as the first two thermal pulses.

The $1.65\,M_\odot$, $Z = 0.02$ track does not show significant third dredge-up because the envelope mass at the first thermal pulse is already relatively small. The stellar model therefore never becomes C-rich (❯ *Fig. 8-12*) and does not experience the associated enhanced mass loss. The $2\,M_\odot$ model has efficient dredge-up, which implies quick increase of the C/O ratio and reduced core growth compared to a sequence with less efficient third dredge-up. Once enhanced mass-loss for C-rich surface composition is activated further core growth will be limited.

■ **Fig. 8-22**

Kippenhahn diagram (as a function of model number) of the He-core flash evolution, He-core burning phase, and following early and thermal-pulse AGB evolution for a $M_{ZAMS} = 1\,M_\odot$, $Z = 0.01$ stellar evolution calculation. The HRD of this track is shown in ❯ *Fig. 8-19*
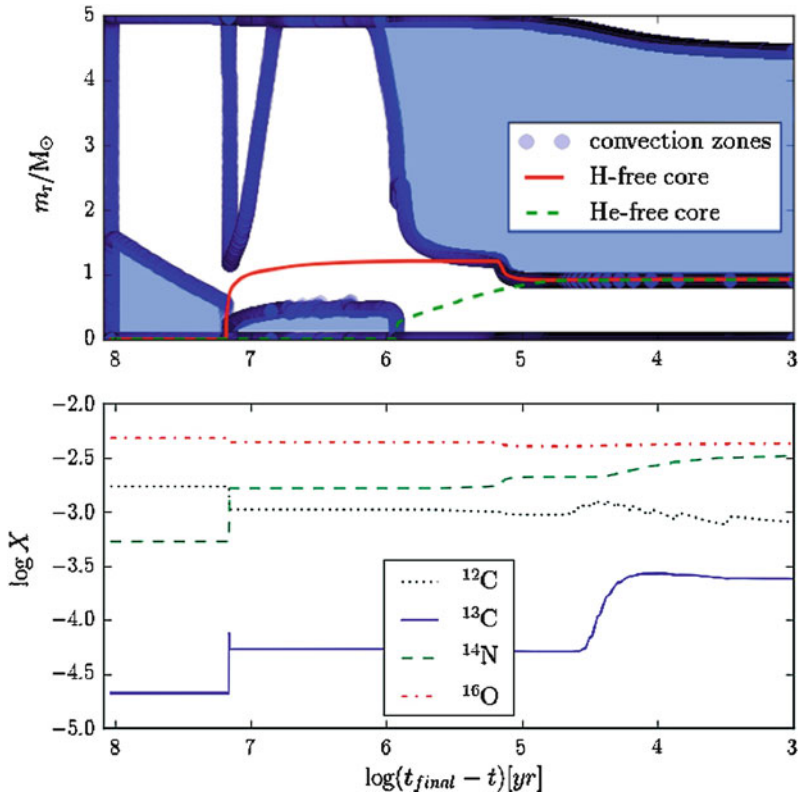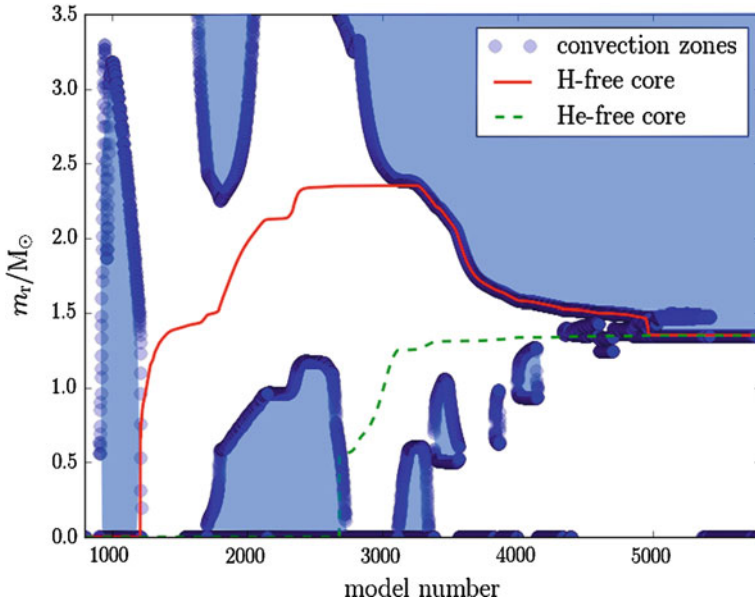
☐ **Fig. 8-23**
Kippenhahn diagram (*top panel*) and surface abundance evolution for a M_{ZAMS} = 5 M$_\odot$, Z = 0.01 stellar evolution calculation. For this mass, the first (log ($t_{final} - t$) = 7.1), second (log ($t_{final} - t$) = 5.1), and the third (log($t_{final} - t$) < 7.24) dredge-ups are present, plus hot-bottom burning is modifying the CNO isotopes during the interpulse phases between He-shell flashes

Massive AGB Stars with Hot-Bottom Burning That Become CO White Dwarfs
At a core mass $\gtrsim$0.8 M$_\odot$, hot-bottom burning sets in and the slope of the MiMf relation changes again. Hot-bottom burning is the colorful name for a situation when the bottom of the convective envelope reaches into the outer layers of the H-burning shell (Boothroyd et al. 1995). As a result, the envelope abundances, in particular of the CNO isotopes, change during the interpulse phase (❷ *Fig. 8-23*). Due to the convectively added fuel, the H-burning shell generates luminosity that is larger than expected from the core-mass luminosity relation (see above and Blöcker and Schönberner 1991).

    ❷ *Figure 8-23* shows the surface abundance evolution for the entire evolution of a 5 M$_\odot$, Z = 0.01 stellar evolution track. The evolution up to the end of He-core burning is similar to that described in detail for the 3 M$_\odot$ case. The effect of the first dredge-up can be seen at log($t_{final} - t$) = 7.1. At the time mark 5.1, the H-free core decreases significantly, and some ^{14}N and ^{4}He (not shown) are mixed into the envelope. This is the second dredge-up which is only found in the more massive AGB stars (❷ *Figs. 8-23* and ❷ *8-24*). Once the thermal-pulse AGB starts, the CNO isotopes show the effect of both third dredge-up and H burning at the

☐ Fig. 8-24
Same as ❯ Fig. 8-22, but showing the ignition of C in after He-core burning in the M_{ZAMS} = 9 M$_\odot$, Z = 0.02 stellar evolution calculation. The central abundance evolution of this track was shown in HRD of this track is shown in ❯ Fig. 8-4

bottom of the envelope. ^{12}C is mixed up and its abundance increases a little bit, only to decrease during the subsequent interpulse by processing into ^{14}N. As a result, the 5 M$_\odot$ stellar model will not become C-rich. The C/O ratio evolution for this case (❯ Fig. 8-12) first shows initially simply small increases of the C/O ratio because, although $\lambda \sim 1$, the total mass that is dredged-up, compared to the envelope mass is simply rather small. The intershell mass decreases with increasing core mass. Only during the last thermal-pulse cycle is a reduction due to hot-bottom burning evident (around $M_\star \sim 2.5$ M$_\odot$).

Characteristic for hot-bottom burning is a ^{12}C/^{13}C ratio close to the (T-dependent) equilibrium value for H burning. In the case shown here, hot-bottom burning is not efficient enough to destroy O. This is however possible in more massive cases and at lower metal content.

The reduced slope of the MiMf in this mass range may be explained by a combination of effects. In hot-bottom burning, part of the fuel is brought into the H-burning shell convectively from the envelope above, while the H-burning ashes are brought back into the envelope. This reduces the amount of He accreted on the CO core and slows the core growth. Models in this mass range also show the largest dredge-up efficiency, further limiting core growth during the thermal-pulse phase.

Progenitors of ONeMg WDs or Electron-Capture Core-Collapse Supernova
If the H-free core exceeds ~1.05 M$_\odot$, C is ignited and O, Ne, and Mg are produced. These are the super-AGB stars (García-Berro and Iben 1994; Siess 2010). The limiting masses for this evolutionary outcome are important for supernova progenitor determinations. Only white dwarfs that form a CO core can explode as a thermonuclear supernova of type Ia. The limiting initial mass for CO core formation is M_{ZAMS} = 7 M$_\odot$ for Z = 0.02 which can be read

off ❷ *Fig. 8-21*. Stars with larger initial mass are not supernova type Ia progenitors. Since the largest core mass with which a CO-white dwarf can form from single star evolution is $1.05\,M_\odot$, the white dwarf will somehow have to gain mass to reach Chandrasekhar mass. This can either happen through accretion and shell burning from a binary companion or via a double degenerate merger. If the initial mass is larger than $M_{ZAMS} = 9\,M_\odot$, the star will ignite C as well as following burning stages under non- or only weakly-degenerate conditions, and the outcome is likely a core-collapse supernova.

For stellar models that just make it over the $\sim1.05\,M_\odot$ core-mass limit (after the second dredge-up), C-ignition takes place off-center in a shell and just like the He-core flash under degenerate conditions. In fact, in the $\rho_c - T_c$ diagram (❷ *Fig. 8-3*), a similar triangle-shaped feature can be observed for the $9\,M_\odot$ track that again signals the C-shell ignition. Whether or not these C-shells always burn all the way to the center is not yet clear. In the case shown in ❷ *Fig. 8-22*, C-ignition takes place in the core, followed by a series of shell flashes that work their way out to the He-free core-mass boundary. During the same time, significant second dredge-up can be seen in the outer layers. The H-free core is reduced from $\sim2.3\,M_\odot$ to just below the Chandrasekhar mass. Around model number 4,500, a small He-shell flash convection zone emerges which gives the second dredge-up a final boost. This feature has been observed in many super-AGB simulations, and it is also called dredge-out (Ritossa et al. 1999; Siess 2007).

Super-AGB stars could in principle end their lives in supernova explosions if the H-free core can grow to the Chandrasekhar mass. Whether or not this can happen depends primarily on the mass loss of the supergiants, as well as on the dredge-up efficiency (Poelarends et al. 2008). The latter depends, again, on the efficiency of convective boundary mixing. If the mass loss is large, the envelope of the super-AGB star is lost quickly, and the core, which is maximally growing at the H-shell burning rate, does not have time to reach Chandrasekhar mass. If convective boundary mixing is efficient, the dredge-up parameter may be $\lambda \sim 1$, and the core does not grow, no matter how low the mass loss is. If the super-AGB stars reaches the Chandrasekhar mass, it will start collapse via electron captures on Mg and Ne. The details of the subsequent supernova explosion are presently investigated.

If the super-AGB star does not explode, it will end its live as a massive ONe white dwarf. Numerous ONe nova have been found (Shore et al. 2003), and for those, obviously, ONe white dwarf must be able to form. Also, the WD mass distribution is now better populated with objects around 1.2–$1.3\,M_\odot$. These could very well be ONe white dwarf.

5   Evolution at Low Metallicity and the Dynamical Star

In ❷ Sect. 2, some limitations of the spherically symmetric stellar evolution assumptions were described. In this section, the status of modeling rotation in AGB stars as well as the phenomenon of dynamic interactions between rapid nuclear energy release via the $^{12}C(p, \gamma)^{13}N$ reaction rate and convective flow will be described.

5.1   Rotation

Rotation will change the evolution of stars in at least three ways. When stars rotate, equipotential and isothermal surfaces in the star may not coincide anymore. Therefore, the direction in which

the temperature gradient points is not always parallel to the direction where gravity points. This leads to global thermal and structural imbalances and deviations from strict spherical symmetry that give rise to large-scale meridional circulations which induces mixing. Mixing will also result, for example, from shear flows in regions of large angular velocity gradients (Maeder and Meynet 2000).

In intermediate-mass stars of low metallicity, these rotation-induced mixing processes are predicted to lift primary ^{12}C and ^{16}O out of the He-burning core (Meynet and Maeder 2002). This material can further mix through the H-burning shell, where most of it will be processed into ^{14}N (see ❯ *Fig. 8-14* for an example of a H-burning shell in an AGB star). According to these models, intermediate-mass stars with even very-low initial metal content would arrive on the thermal-pulse AGB with an envelope CNO abundance that is only 1 dex below solar. This would have implications for, and in fact may prevent, the occurrence of the H-ingestion events in low-metallicity thermal-pulse AGB stars.

Rotation, as well as other mixing mechanisms, have been investigated as sources for extra-mixing below that envelope convection zone that is required to explain the abundance evolution along the RGB and (early-)AGB (e.g., Denissenkov and VandenBerg 2003; Palacios et al. 2006; Charbonnel and Lagarde 2010).

Rotation will effect the way the *s* process operates in thermal-pulse AGB stars (Langer et al. 1999; Herwig et al. 2003; Siess et al. 2004). The current models do not induce enough mixing at the end of the third dredge-up to account quantitatively for the size of the ^{13}C pocket (see ❯ Sect. 3.2.2). In addition, present models of rotating AGB stars predict too much mixing in the ^{13}C pocket which would lead to a poisoning of the *s*-process neutron source via the admixture of ^{14}N and the ^{14}N$(n, p)^{14}$C reaction. This large amount of mixing at the core-envelope interface may be the result of a too large angular velocity gradient resulting from inefficient angular momentum transport during the previous evolution. The fact that observed white dwarfs rotate much slower than the cores of rotating tip-AGB star models (Suijs et al. 2008) points in the same direction of missing angular momentum transport mechanisms in present models of rotating stars. However, a significantly reduced amount of rotation-induced mixing at the core-envelope boundary may in fact help to account for the observed spread in neutron exposure for stars of a given initial mass and metallicity (Herwig 2005).

5.2 Dynamic Interaction of Nuclear Burning with Convection

The most important difference for the evolution of stars at very low or even zero metal content is the reduced availability of CNO material that either prevents or limits the efficiency of the CNO-cycle mode of H burning. As a result, to make better use of what is available, the CNO cycle will operate at higher temperature to recycle the available CNO material more often.

If the metal content is indeed zero (Pop. III), then H burning will proceed via the PP chains. At higher masses, this will require such large temperatures that even during H-core burning at some point trace amounts of ^{12}C appear from triple-α reaction.

When H burns at higher temperature, it is closer, in terms of entropy, to the conditions in the He shell. One of the themes of stellar evolution at extremely low metal content ($Z \lesssim 10^{-4}$) is frequent encounters of H-combustion events. These are all events in which in one way or another protons get mixed with primary ^{12}C at convective velocities. Such instances have been reported in stellar evolution calculations of solar and intermediate-mass stars of very-low metal content for many decades, for example, in the He-core flash during which H-rich material from

the unprocessed envelope above is ingested into the ^{12}C-rich layer underneath (Fujimoto et al. 2000; Weiss et al. 2004). A similar scenario are the AGB He-shell flashes (Iwamoto et al. 2004; Campbell and Lattanzio 2008), where again H ingestion in the He-shell flash has been found. Closely related phenomena have been observed during the third dredge-up in metal-poor AGB stars, where the convective boundary mixing induced to facilitate dredge-up and ^{13}C causes a vicious feedback from protons reacting with ^{12}C on the mixing time scale. This hot dredge-up is quantitatively not understood and limits the accuracy of simulation predictions at these low metallicities (Herwig 2004; Goriely and Siess 2004).

All these events are characterized by an interaction of the rapid nuclear energy release by ^{12}C$(p, \gamma)^{13}$N as well as the β-decay of ^{13}N and the hydrodynamics and turbulence of the convective flow. The regime can be identified in terms of the Damköhler number (Dimotakis 2005):

$$D_\alpha = \frac{\tau_{\text{mix}}}{\tau_{\text{react}}} \tag{8.9}$$

where τ_{mix} represents the mixing time scale, which can be estimated from mixing-length theory in the convection zone as the convective turnover time scale. τ_{react} is the reaction time scale, and can be estimated for each reaction, for example, for the ^{12}C(p, γ) reaction by

$$\tau_{^{12}\text{C}}(p) = \frac{12}{X(^{12}\text{C})\rho N_A < \sigma v >} \tag{8.10}$$

where 12 is the mass number of ^{12}C, X is the mass fraction of ^{12}C, ρ density, and $N_A < \sigma v >$ is the Avogadro number times the reaction rate, as, for example, tabulated for many charged particle reactions by Angulo et al. (1999).

If $D_\alpha \ll 1$, then nuclear burning is slow compared to mixing, and the convection zone is always well mixed. This would be, for example, the situation during H-core burning. However, if $D_\alpha \sim 1$ burning and advective flows are on the same time scale and will effect each other if the amount of energy released in the reactions is dynamically relevant. The reaction rate increases strongly with temperature. At $T \sim 1.5 \times 10^8$ K and $\rho \sim 10^3$g/cm^3, $\tau_{\text{mix}} \sim \tau_{\text{react}} \sim 15$ min. The temperature corresponds to a location approximately halfway between the location where the H ingestion takes place ($T < 10^8$ K) and where the He burning takes place ($T \sim 3 \times 10^8$ K).

The main problem of these H-combustion events is that it is unlikely that they can be correctly described with the mixing model (mixing-length theory) presently used in many spherical stellar evolution codes (see discussion in ❯ Sect. 2). Mixing-length theory uses time and spatial averages over times and scales that are much longer/larger than the scales of significant nuclear energy release on the convective turnover time scale. The key question, that spherically symmetric simulations cannot answer, is how distributed and inhomogeneous the nuclear energy release is on large scales. The more inhomogeneous the burn is due to inhomogenous distribution of H-fuel enriched downdrafts, the less spherically symmetric is the situation. Another key question concerns the width of the burning flame that depends on the velocity distribution of H-fuel enriched downdrafts.

In the previous section, the H-ingestion evolution of very-late thermal-pulse stars was described. It is triggered by a He-shell flash that happens after the post-AGB star has evolved around the knee, but before, it has cooled down so much that it cannot support nuclear burn anymore at all. These post-AGB H-ingestion flash stars perform the same type of event as their very-low-metallicity counterparts. The advantage of the post-AGB stars is that for some of them, most notably Sakurai's object, excellent observational information of the real-time evolution
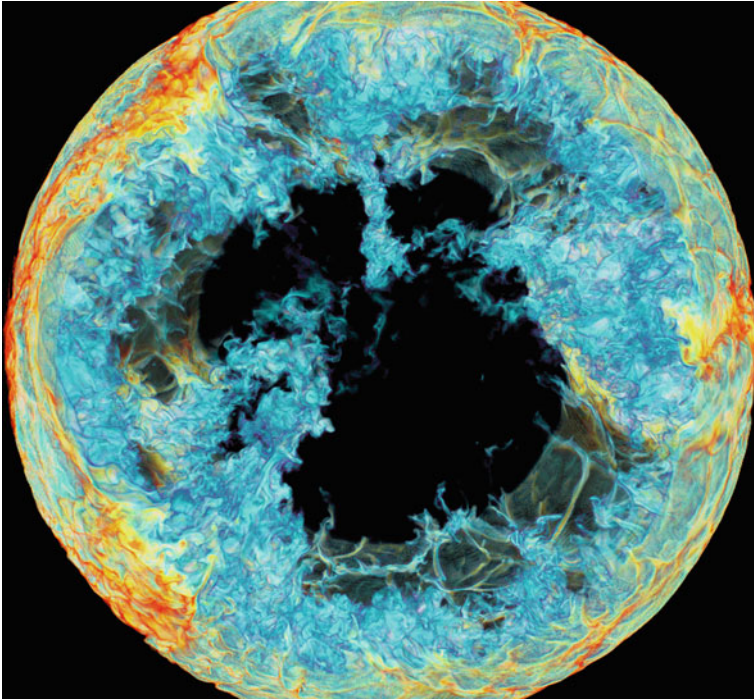
◼ **Fig. 8-25**
Concentration (fractional volume) of H-rich material being entrained and ingested into the He-shell flash convection zone of a pre-white dwarf (born-again) model at a relatively early time (278 min). This 3D simulation was performed on a 768³ grid with Paul Woodward's PPMstar code. It aims to reproduce the conditions of the H-ingestion flash that occurred in post-AGB star Sakurai's object. The stratification is almost identical to stellar evolution model 4908 from Herwig et al. (2011). The color scale is chosen so that concentration levels above $\sim 10^{-3.5}$ are transparent. *Yellow* corresponds to concentration $\sim 10^{-4}$, *white* $\sim 10^{-5}$, and *light blue* $\sim 10^{-6}$

and surface abundance changes is available. These can be used to validate multi-physics simulations of the nucleosynthesis of the H-combustion phenomenon. Such a program is presently underway (Herwig et al. 2011).

A snapshot from a hydrodynamic simulation of the entrainment and subsequent nuclear burning of H into the He-shell flash convection zone is shown in ❯ *Fig. 8-25*. The simulation aims to reproduce specifically the conditions of Sakurai's object when it erupted in 1996. One of the most obvious but also most important differences between 3D and 1D simulations of such phases is that in 1D, the H-rich material is represented by one number for the entire 4π sphere according to the assumption of spherical symmetry. Contrary to that, the 3D simulation shown in ❯ *Fig. 8-25* reveals large-scale inhomogeneities during this early stage of the H entrainment. The energy generation follows the composition distribution and they both will be patchy and spotty. While 1D simulations predict that the energy should be released in a very well-defined and thin layer, the 3D picture suggests that a more regional, variable, and time-dependent nuclear burning mode is possible under certain circumstances. The spherically symmetric burn

of the 1D simulations would predict that the energy release from H-combustion would quickly prohibit mixing from the outer parts of the convection zone to the hottest layers where neutrons can be released. Investigations based on hydrodynamic simulations such as those shown in ❯ *Fig. 8-25* will eventually clarify the properties of H combustion in stellar evolution. This will greatly improve the fidelity of simulations and yield prediction of stars with very low or even zero metal content that were formed in the early universe.

Acknowledgments

References

Angulo, C., Arnould, M., & Rayet, M. et al. 1999, Nucl. Phys. A, 656, 3, NACRE compilation

Arlandini, C., Käppeler, F., Wisshak, K., Gallino, R., Lugaro, M., Busso, M., & Straniero, O. 1999, ApJ, 525, 886

Arndt, T., Fleischer, A., & Sedlmayr, E. 1997, A&A, 327, 614

Arnett, D., Meakin, C., & Young, P. A. 2010, ApJ, 710, 1619

Arnould, M., Goriely, S., & Jorissen, A. 1999, A&A, 347, 572

Asplund, M., Lambert, D. L., Kipper, T., Pollacco, D., & Shetrone, M. D. 1999, A&A, 343, 507

Asplund, M., Grevesse, N., Sauval, A. J., & Scott, P. 2009, ARA&A, 47, 481

Bisterzo, S., Gallino, R., Straniero, O., Cristallo, S., & Käppeler, F. 2010, MNRAS, 404, 1529

Blöcker, T. 1993, PhD thesis, Universität Kiel

Blöcker, T. 1995a, A&A, 297, 727

Blöcker, T. 1995b, A&A, 299, 755

Blöcker, T., & Schönberner, D. 1991, A&A, 244, L43

Blöcker, T., & Schönberner, D. 1997, A&A 324, 991

Böhm-Vitense, E. 1958, Z. Astrophys., 46, 108

Boothroyd, A. I., Sackmann, I.-J., & Wasserburg, G. J. 1995, ApJL, 442, L21

Brown, T. M., Sweigart, A. V., Lanz, T., Landsman, W. B., & Hubeny, I. 2001, ApJ, 562, 368

Browning, M. K., Brun, A. S., & Toomre, J. 2004, ApJ, 601, 512

Brun, A. S., & Palacios, A. 2009, ApJ, 702, 1078

Busso, M., Gallino, R., & Wasserburg, G. J. 1999, ARA&A, 37, 239

Busso, M., Gallino, R., Lambert, D. L., Travaglio, C., & Smith, V. V. 2001, ApJ, 557, 802

Campbell, S. W., & Lattanzio, J. C. 2008, A&A, 490, 769

Canuto, V. M. 2011, A&A, 528, A77

Canuto, V. M., Goldman, I., & Mazzitelli, I. 1996, ApJ, 473, 550

Catalán, S., Isern, J., García-Berro, E., & Ribas, I. 2008, MNRAS, 387, 1693

Charbonnel, C., & Lagarde, N. 2010, A&A, 522, A10

Charbonnel, C., & Zahn, J. 2007, A&A, 467, L15

Clarke, C. J., & Carswell, R. F. 2003, Principles of Astrophysical Fluid Dynamics (Cambridge: Cambridge University Press)

Clayton, D. D. 1968, Principles of Stellar Evolution and Nucleosynthesis (Chicago: University of Chicago Press)

Clayton, G. C., Geballe, T. R., Herwig, F., Fryer, C., & Asplund, M. 2007, ApJ, 662, 1220

Cox, J. P., & Giuli, R. T. 1968, Principles of Stellar Structure (New York: Gordon and Breach)

Cristallo, S., Straniero, O., Lederer, M. T., & Aringer, B. 2007, ApJ, 667, 489

Cristallo, S., Piersanti, L., Straniero, O., Gallino, R., Domínguez, I., Abia, C., Di Rico, G., Quintini, M., & Bisterzo, S. 2011, ApJS, 197, 17

De Beck, E., Decin, L., de Koter, A., Justtanont, K., Verhoelst, T., Kemper, F., & Menten, K. M. 2010, A&A, 523, A18

Denissenkov, P. A. 2010, ApJ, 723, 563

Denissenkov, P. A., & Merryfield, W. J. 2011, ApJL, 727, L8

Denissenkov, P. A., & VandenBerg, D. A. 2003, ApJ, 593, 509

Dimotakis, P. E. 2005, Annu. Rev. Fluid Mech., 37, 329

Driebe, T., Schönberner, D., Blöcker, T., & Herwig, F. 1998, A&A, 339, 123

Duerbeck, H. W., & Benetti, S. 1996, ApJ Lett., 468, L111

Endal, A. S., & Sofia, S. 1976, ApJ, 210, 184

Ferrario, L., Wickramasinghe, D., Liebert, J., & Williams, K. A. 2005, MNRAS, 361, 1131

Forestini, M., & Charbonnel, C. 1997, A&AS, 123, 241

Freiburghaus, C., Rosswog, S., & Thielemann, F.-K. 1999, ApJL, 525, L121

Freytag, B., & Höfner, S. 2008, A&A, 483, 571

Frost, C. A., & Lattanzio, J. C. 1996, ApJ, 473, 383

Fryer, C. L., Herwig, F., Hungerford, A., & Timmes, F. X. 2006, ApJ Lett., 646, L131

Fujimoto, M. Y. 1977, PASJ, 29, 331

Fujimoto, M. Y., Ikeda, Y., & Iben, I., J. 2000, ApJ Lett., 529, L25

Gallino, R., Arlandini, C., Busso, M., Lugaro, M., Travaglio, C., Straniero, O., Chieffi, A., & Limongi, M. 1998, ApJ, 497, 388

García-Berro, E., & Iben, I., Jr. 1994, ApJ, 434, 306

Goriely, S., & Siess, L. 2004, A&A, 421, L25

Groenewegen, M. A. T., & de Jong, T. 1993, A&A, 267, 410

Groenewegen, M. A. T., & de Jong, T. 1998, A&A, 337, 797

Gustafsson, B., & Höfner, S. 2003, in Astronomy and Astrophysics Library, Asymptotic Giant Branch Stars, ed. H. J. Habing & H. Olofsson (New York/Berlin: Springer)

Habing, H. J., & Olofsson, H. (eds.) 2004, Astronomy and Astrophysics Library, Asymptotic Giant Branch Stars (New York/Berlin: Springer)

Hajduk, M., Zijlstra, A. A., Herwig, F., van Hoof, P. A. M., Kerber, F., Kimeswenger, S., Pollacco, D. L., Evans, A., Lopéz, J. A., Bryce, M., Eyres, S. P. S., & Matsuura, M. 2005, Science, 308, 231

Hansen, C. J., Kawaler, S. D., & Trimble, V., ed. 2004, Stellar Interiors : Physical Principles, Structure, and Evolution (Springer-Verlag)

Henyey, L. G., Forbes, J. E., & Gould, N. L. 1964, ApJ, 139, 306

Herwig, F. 2000, A&A, 360, 952

Herwig, F. 2001a, ApJ Lett., 554, L71

Herwig, F. 2001b, APSS, 275, 15

Herwig, F. 2004, ApJ, 605, 425

Herwig, F. 2005, ARAA, 43, 435

Herwig, F., & Austin, S. M. 2004, ApJ Lett., 613, L73

Herwig, F., Blöcker, T., Schönberner, D., & El Eid, M. F. 1997, A&A, 324, L81

Herwig, F., Schönberner, D., & Blöcker, T. 1998, A&A, 340, L43

Herwig, F., Blöcker, T., Langer, N., & Driebe, T. 1999, A&A, 349, L5

Herwig, F., Langer, N., & Lugaro, M. 2003, ApJ, 593, 1056

Herwig, F., Austin, S. M., & Lattanzio, J. C. 2006a, Phys. Rev. C., 73, 025802

Herwig, F., Freytag, B., Hueckstaedt, R. M., & Timmes, F. X. 2006b, ApJ, 642, 1057

Herwig, F., Freytag, B., Fuchs, T., Hansen, J. P., Hueckstaedt, R. M., Porter, D. H., Timmes, F. X., & Woodward, P. R. 2007, in Astronomical Society of the Pacific Conf. Ser. 378, Why Galaxies Care About AGB Stars: Their Importance as Actors and Probes, ed. F. Kerschbaum, C. Charbonnel, & R. F. Wing , 43 (San Francisco, CA: ASP)

Herwig, F., Pignatari, M., Woodward, P. R., Porter, D. H., Rockefeller, G., Fryer, C. L., Bennett, M., & Hirschi, R. 2011, ApJ, 727, 89

Hinkle, K. H., Lebzelter, T., Joyce, R. R., Ridgway, S., Close, L., Hron, J., & Andre, K. 2008, A&A, 479, 817

Hofmeister, E., Kippenhahn, R., & Weigert, A. 1964, Z. Astrophys., 59, 215

Hollowell, D., & Iben, I., Jr. 1988, ApJ, 333, L25

Iben, I. Jr. 1981, ApJ, 246, 278

Iben, I., Jr., & MacDonald, J. 1995, in LNP No. 443, White Dwarfs, ed. D. Koester & K. Werner (Heidelberg: Springer), 48

Iben, I., Jr., Kaler, J. B., Truran, J. W., & Renzini, A. 1983, ApJ, 264, 605

Iglesias, C. A., & Rogers, F. J. 1996, ApJ, 464, 943

Iliadis, C. 2007, Nuclear Physics of Stars (Weinheim: Wiley)

Iwamoto, N., Kajino, T., Mathews, G. J., Fujimoto, M. Y., & Aoki, W. 2004, ApJ, 602, 378

Jeffery, C. S., & Schönberner, D. 2006, A&A, 459, 885

Jura, M., & Kleinmann, S. G. 1989, ApJ, 341, 359

Jura, M., & Kleinmann, S. G. 1992, ApJS, 83, 329

Käppeler, F., Beer, H., & Wisshak, K. 1989, Rep. Prog. Phys., 52, 945

Käppeler, F., Gallino, R., Bisterzo, S., & Aoki, W. 2011, Rev. Mod. Phys., 83, 157

Karakas, A. I. 2010, MNRAS, 403, 1413

Karakas, A. I., Lattanzio, J. C., & Pols, O. R. 2002, PASA, 19, 515

Kippenhahn, R., & Weigert, A. 1990, Stellar Structure and Evolution (Berlin: Springer)

Kroupa, P. 2002, Science, 295, 82

Langer, N., Heger, A., Wellstein, S., & Herwig, F. 1999, A&A, 346, L37

Lattanzio, J. C. 1986, ApJ, 311, 708

Lattanzio, J. C. 1989, ApJ, 344, L25

Lawlor, T. M., & MacDonald, J. 2003, ApJ, 583, 913

Liebert, J., Bergeron, P., & Holberg, J. B. 2005, ApJS, 156, 47

Lugaro, M. 2005, World Scientific Series in Astronomy and Astrophysics, Stardust from Meteorites. An Introduction to Presolar Grains, Vol. 9 (London/Singapore: World Scientific)

Lugaro, M., Herwig, F., Lattanzio, J. C., Gallino, R., & Straniero, O. 2003, ApJ, 586, 1305

Maeder, A., & Meynet, G. 2000, ARA&A, 38, 143

Maeder, A., & Meynet, G. 2012, Rev. Mod. Phys., 84, 25

Marigo, P. 2000, A&A, 360, 617

Marigo, P. 2001, A&A, 370, 194

Marigo, P. 2002, A&A, 387, 507

Marigo, P., & Aringer, B. 2009, A&A, 508, 1539

Marigo, P., Bressan, A., & Chiosi, C. 1996, A&A, 313, 545

Marigo, P., Girardi, L., & Bressan, A. 1999, A&A, 344, 123

Mattsson, L., Wahlin, R., & Höfner, S. 2010, A&A, 509, A14

Meyer, B. S. 1994, ARA&A, 32, 153

Meynet, G., & Maeder, A. 2002, A&A, 390, 561

Miller Bertolami, M. M., Althaus, L. G., Serenelli, A. M., & Panei, J. A. 2006, A&A, 449, 313

Mowlavi, N. 1999, A&A, 344, 617

Olofsson, H. 2003, in Astronomy and Astrophysics library, Asymptotic Giant Branch Stars, ed. H. J. Habing & H. Olofsson (New York, Berlin: Springer)

Olofsson, H., González Delgado, D., Kerschbaum, F., & Schöier, F. L. 2002, A&A, 391, 1053

Paczyński, B. 1970, Acta Astron., 20, 47

Palacios, A., Charbonnel, C., Talon, S., & Siess, L. 2006, A&A, 453, 261

Passy, J.-C., De Marco, O., Fryer, C. L., Herwig, F., Diehl, S., Oishi, J. S., Mac Low, M.-M., Bryan, G. L., & Rockefeller, G. 2012, ApJ, 744, 52

Pauldrach, A., Puls, J., Kudritzki, R. P., Mendez, R. H., & Heap, S. R. 1988, A&A, 207, 123

Paxton, B., Bildsten, L., Dotter, A., Herwig, F., Lesaffre, P., & Timmes, F. 2011, ApJS, 192, 3

Pinsonneault, M. 1997, ARA&A, 35, 557

Poelarends, A. J. T., Herwig, F., Langer, N., & Heger, A. 2008, apj, 675, 614

Porter, D. H., & Woodward, P. R. 2000, ApJS, 127, 159

Renzini, A., & Voli, M. 1981, A&A, 94, 175

Ricker, P. M., & Taam, R. E. 2008, ApJL, 672, L41

Ritossa, C., García-Berro, E., & Iben, I. J. 1999, ApJ, 515, 381

Rolfs, C. E., & Rodney, W. S. 1988, Cauldrons in the Cosmos: Nuclear Astrophysics (Chicago: University of Chicago Press)

Schaller, G., Schaerer, D., Meynet, G., & Maeder, A. 1992, A&AS, 96, 269

Schönberner, D. 1981, A&A, 103, 119

Serenelli, A., & Weiss, A. 2005, A&A, 442, 1041

Shore, S. N., Schwarz, G., Bond, H. E., Downes, R. A., Starrfield, S., Evans, A., Gehrz, R. D., Hauschildt, P. H., Krautter, J., & Woodward, C. E. 2003, AJ, 125, 1507

Siess, L. 2007, A&A, 476, 893

Siess, L. 2010, A&A, 512, A10+

Siess, L., Goriely, S., & Langer, N. 2004, A&A, 415, 1089

Sneden, C., Cowan, J. J., & Gallino, R. 2008, ARAA, 46, 241

Straniero, O., Gallino, R., Busso, M., Chieffi, A., Raiteri, C. M., Salaris, M., & Limongi, M. 1995, ApJ, 440, L85

Straniero, O., Cristallo, S., & Gallino, R. 2009, PASA, 26, 133

Suijs, M. P. L., Langer, N., Poelarends, A.-J., Yoon, S.-C., Heger, A., & Herwig, F. 2008, A&A, 481, L87

Thompson, M. J., Christensen-Dalsgaard, J., Miesch, M. S., & Toomre, J. 2003, ARAA, 41, 599

Timmes, F. X., Woosley, S. E., & Weaver, T. A. 1995, APJS, 98, 617

Travaglio, C., Gallino, R., Arnone, E., Cowan, J., Jordan, F., & Sneden, C. 2004, ApJ, 601, 864

van Loon, J. T. 2005, Stellar Evolution at Low Metallicity: Mass Loss, Explosions, Cosmology. ASP Conf. Ser. 353, Proceedings of the Conference Held 15-19 August, 2005 in Tartu, Estonia, (San Francisco, CA: ASP) p. 211. ArXiv Astrophysics e-prints

van Loon, J. T., Groenewegen, M. A. T., de Koter, A., Trams, N. R., Waters, L. B. F. M., Zijlstra, A. A., Whitelock, P. A., & Loup, C. 1999, A&A, 351, 559

van Loon, J. T., Cioni, M.-R. L., Zijlstra, A. A., & Loup, C. 2005, A&A, 438, 273

van Winckel, H. 2003, ARAA, 41, 391

VandenBerg, D. A., Bergbusch, P. A., & Dowler, P. D. 2006, ApJS, 162, 375

Vassiliadis, E., & Wood, P. 1993, ApJ, 413, 641

Venn, K. A., Irwin, M., Shetrone, M. D., Tout, C. A., Hill, V., & Tolstoy, E. 2004, AJ, 128, 1177

Wachter, A., Schröder, K.-P., Winters, J. M., Arndt, T. U., & Sedlmayr, E. 2002, A&A, 384, 452

Ward, R. A., & Fowler, W. A. 1980, ApJ, 238, 266

Weidemann, V. 2000, A&A, 363, 647

Weiss, A., & Ferguson, J. W. 2009, A&A, 508, 1343

Weiss, A., Schlattl, H., Salaris, M., & Cassisi, S. 2004, A&A, 422, 217

Werner, K., & Herwig, F. 2006, PASP, 118, 183

Willson, L. A. 2000, ARAA, 38, 573

Xiong, D. R., Cheng, Q. L., & Deng, L. 1997, ApJS, 108, 529

Yoon, S.-C., Langer, N., & van der Sluys, M. 2004, A&A, 425, 207

Zinner, E. 1998, Ann. Rev. Earth Planet. Sci., 26, 147